Oxidation state and coordination of Fe in minerals: An Fe K–XANES spectroscopic study

5 authors, including:

Francois Farges
Muséum National d'Histoire Naturelle
172 PUBLICATIONS **6,000** CITATIONS

P. E. Petit
Institut des Materiaux Jean Rouxel
35 PUBLICATIONS **1,791** CITATIONS

Gordon Brown
Stanford University
396 PUBLICATIONS **24,919** CITATIONS

François Martin
French National Centre for Scientific Research
100 PUBLICATIONS **2,988** CITATIONS

Some of the authors of this publication are also working on these related projects:

Interface Physics View project

Historical gems/mineralogy and history View project

Oxidation state and coordination of Fe in minerals: An Fe *K*-XANES spectroscopic study

MAX WILKE,[1,*] FRANÇOIS FARGES,[1,2] PIERRE-EMMANUEL PETIT,[3] GORDON E. BROWN JR.,[2,4] AND FRANÇOIS MARTIN[5]

[1]Laboratoire des géomatériaux, Université de Marne-la-Vallée, 77454 Marne la Vallée Cedex, France
[2]Department of Geological and Environmental Sciences, Stanford University, Stanford, California 94305-2115, U.S.A.
[3]European Synchrotron Radiation Facility BP 220, 38043 Grenoble Cedex, France
[4]Stanford Synchrotron Radiation Laboratory, SLAC, P.O. Box 4349, Stanford University, Stanford, California 94309, U.S.A.
[5]Équipe Géomarg, Université Paul Sabatier–UMR CNRS 5563 39 Allées Jules Guesde, 31000 Toulouse, France

ABSTRACT

High-resolution Fe K-edge XANES spectra of a series of crystalline Fe^{2+}- and Fe^{3+}-bearing model compounds were measured in an effort to correlate characteristics of the pre-edge feature with oxidation state and local coordination environment of Fe atoms. The model compounds comprise 30 natural minerals and synthetic compounds, with Fe coordination environments ranging from 4 to 12 O atoms for Fe^{2+}, including 5-coordinated trigonal bipyramidal Fe^{2+}, and from 4 to 6 O atoms for Fe^{3+}. Most pre-edge spectra show two components (due to crystal-field splitting) that are located just above the Fermi level.

The most useful characteristics of the Fe-K pre-edge for determining Fe oxidation state and coordination number are the position of its centroid and its integrated intensity. The separation between the average pre-edge centroid positions for Fe^{2+} and Fe^{3+} is 1.4 ± 0.1 eV. Thus, the position of the pre-edge feature can be used as a measure of the average Fe-redox state, with the average pre-edge position for mixed Fe^{2+}-Fe^{3+} compounds occurring between positions for Fe^{2+} and Fe^{3+}. The lowest pre-edge normalized heights and integrated intensities are observed for the most centrosymmetric sites of Fe, in agreement with previous studies (see Waychunas et al. 1983). Examination of the pre-edge features of mechanical mixtures of phases containing different proportions of Fe^{2+} and Fe^{3+} suggests that the pre-edge position and intensity for these mixtures can vary quite non-linearly with the average redox state of Fe. However, distinctly different trends of pre-edge position vs. pre-edge intensity can be observed, depending on the coordination environment of Fe^{2+} and Fe^{3+}, with an accuracy in redox determination of ± 10 mol% provided that the site geometry for each redox state is known. These methods have been used to estimate the Fe^{3+}/Fe^{2+} ratio in 12 minerals (magnetite, vesuvianite, franklinite, rhodonite, etc.) containing variable/unknown amounts of Fe^{2+}/Fe^{3+}.

INTRODUCTION

Iron is the most important transition element in minerals and silicate melts. However, depending on redox conditions during the formation, Fe^{3+}/Fe^{2+} ratios can vary significantly. Quantitative determination of the redox state of Fe is essential for constraining the thermodynamic conditions under which rocks and magma formed (see, e.g., Wood and Virgo 1989; Parkinson and Arculus 1997). Mössbauer spectroscopy has been widely used to measure these redox states in mineralogically and geochemically relevant phases (e.g., Dyar 1985; Mysen 1991; McCammon 1997; Dunlap et al. 1998; Wilke et al. 1999; Rossano et al. 1999 among others). However, this method is challenging in the case of small samples (e.g., micrometer sized: see Sobolev et al. 1999) or in natural samples with dilute levels of Fe (i.e., below 1 wt%, due to the relatively low natural abundance (2.1 isotopic%) of ^{57}Fe). In addition, there have been

several electron energy loss spectroscopy (EELS) studies at the L-, and M-edges of iron in model compounds in order to derive Fe-oxidation state information (Garvie and Busek 1998; van Aken et al. 1998, 1999). However, this method requires high vacuum conditions, which prohibits in-situ experiments at high temperature and/or high pressure.

X-ray absorption fine structure (XAFS) spectroscopy is sensitive to Fe redox states, especially the pre-edge feature, which is located ~15–20 eV before the main K-edge crest of Fe (see Waychunas et al. 1983). Pre-edges are related to 1s → 3d (quadrupolar) and/or to 1s → 4p (dipolar) metal electronic transitions (Dräger et al. 1988; Westre et al. 1997; Heumann et al. 1997). The pre-edge position shifts towards higher energy with increasing oxidation state (White and McKinstry 1966; Srivastava and Nigam 1973). During the past few years, the Fe pre-K-edge position has been used to determine the redox state of Fe in a number of earth materials, including weathered magnetites (Bajt et al. 1994), biotite (Heald et al. 1995), oxidized olivines (Dyar et al. 1998), amphiboles (Delaney et al. 1996b), and glasses (Delaney et al. 1996a; Galoisy et al. 2001). In addition, Delaney et al. (1998) demonstrated that this method may

* Present address: Institut für Geowissenschaften Universität Potsdam Postfach 601553 14415 Potsdam, Germany. E-mail: max@geo.uni-potsdam.de

be applied to almost all mineral groups containing Fe in six-fold coordination. In contrast to XANES measurements at the Fe K-edge, which can be carried out under in situ conditions, including high temperatures and pressures and on samples containing Fe at the ppm level, XANES or EELS (or ELNES) measurements at the Fe $L_{2/3}$-edge (see Cressey et al. 1993; Garvie and Buseck 1998; van Aken et al. 1998) or at the Fe $M_{2,3}$-edge (van Aken et al. 1999) require ultra-high vacuum conditions. However, using XANES K-edge spectroscopy, these small features (only a few percentages of the edge height) are not easy to measure accurately, especially when iron is dilute. In addition, XAFS spectroscopy can provide direct structural information for the first and more distant neighboring atoms around Fe.

New high-flux insertion device beamlines at second- and third-generation synchrotron light sources make this method more applicable to samples dilute in Fe (see Newville et al. 1998; Gauthier et al. 1999). In addition, these beamlines permit spectra to be collected with energy resolution close to the core-hole lifetime limit due to lower experimental broadening than was possible in past studies using older beamlines, resulting in more accurate determination of the oxidation state and local coordination environment of iron.

This study presents the results of a high-resolution XANES spectroscopy study of Fe^{2+} and Fe^{3+} in 30 minerals that possess a wide range of coordination environments for Fe. The speciation of Fe (oxidation state and coordination environment) in these minerals was examined using correlations between the normalized integrated intensity and the centroid of the energy position of pre-edge features. The conclusions from this study are qualitatively similar to those reported earlier by Waychunas et al. (1983) and Galoisy et al. (2001). In addition, this study also provides new information for the trigonal bipyramidal coordination environment of Fe^{2+}, observed in silicate glasses (Brown et al. 1995). To determine the sensitivity of pre-edge intensity and energy position to Fe oxidation state and coordination number, we report Fe-K pre-edge data for mixtures of phases with differing amounts of $^{IV}Fe^{2+}$, $^{VI}Fe^{2+}$, $^{IV}Fe^{3+}$, and $^{VI}Fe^{3+}$. The results show that there is considerable non-linearity in the variation of the pre-edge position if both Fe-redox state and coordination vary simultaneously. Our methods are used to analyze 14 Fe-bearing minerals of known crystal structure and cation site geometries to test our method in determining their Fe^{2+}/Fe^{3+} ratios.

EXPERIMENTAL METHODS

Model compounds

Tables 1a and 1b list the crystalline model compounds used here for characterising Fe^{2+} and Fe^{3+} in the various coordination environments. The reference column indicates previous studies of similar (or the identical) mineral.

XAFS data collection

Pre-edge and XANES spectra at the Fe K-edge were collected at the European Synchrotron Radiation Facility (ESRF, Grenoble, France), on the new undulator beamline ID26 (Gauthier et al. 1999; Solé et al. 1999). The storage ring oper-
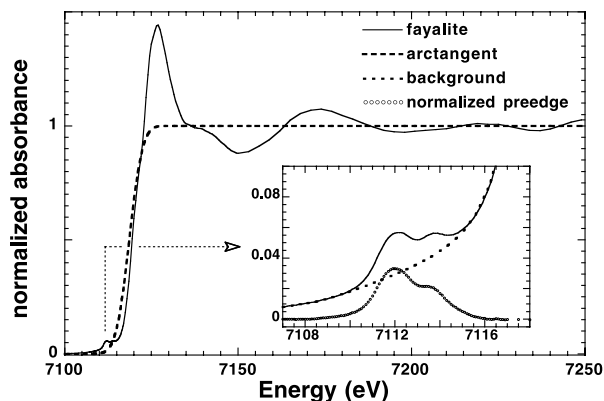
FIGURE 1. Method used for background normalization. The arctangent function is schematic in this figure, representing the atomic absorption curve normalized between 0 and 1. Spectra were modeled before the edge using a Victoreen function and normalized in atomic absorption, based on the average absorption coefficient between 7200 and 7300 eV. The pre-edge background was modeled using an interpolation function (spline function) using data a few eV before and after the pre-edge.

ating conditions were 6 GeV electron energy and 150–185 mA electron current. The used beam size at the sample position was 80×200 μm². A Si(220) double-crystal monochromator was used for these experiments. Its energy resolution is ~0.4 eV at the Fe K-edge. However, the main limitation for energy resolution is the finite core-hole width of the absorbing element (~1.15 eV at the Fe K-edge; Krause and Oliver 1979), resulting in a convoluted energy resolution (FWHM) of ~1.4 eV (see below). A resolution analysis performed at the Ni K-edge on the same ESRF spectrometer (Farges et al. unpublished manuscript) indicates that the spectra were collected under energy resolution conditions close to the maximum currently possible. For all experiments, a reference foil (usually metallic Fe) was used to provide an accurate, internal energy calibration of the monochromator for all spectra (first inflection point of the Fe K-edge set at 7111.08 eV). This value is based on a calibration of the Cu-foil K-edge first inflection point at 8983.32 eV (see Pettifer and Hermes 1985). The energy reproducibility for these experiments is ±0.05 eV. Two mirrors were used to remove the high-energy harmonics from the incident X-ray beam (energy cut-off at 10 keV). XAFS data for most model compounds were collected in the transmission mode as well as in the fluorescence mode with the sample positioned normal to the beam to minimize self-absorption effects (Tröger et al. 1992). Optimum sample thicknesses for transmission experiments were calculated using the computer code "absorbance 2.1" (written by F. Farges) to result in an absorbance (μ) and an edge jump (Δμ/μ) close to 1 at 7.2 keV (typical thicknesses are 5 to 30 μm depending on Fe concentration). The appropriate amounts of powdered model compounds (size fraction below 50 μm) were mixed with boron nitride to reach a dilution level for the sample dimensions corresponding to the calculated theoretical thickness. Each mixture was compressed into a pellet and loaded into a Teflon sample holder. For the model

TABLE 1a. Model compounds for Fe^{2+}

Sample	Chemical formula	wt% FeO	CN Symmetry	Origin	References
gillespite	$BaFeSi_4O_{10}$		4 D_{4h}	Tres Pozos, Baja Calif., Mexico	Pabst 1959
staurolite*	$Fe_{1.5}Mg_{0.5}Al_9Si_{3.9}Al_{0.1}O_{22}(OH)_2$	13.1	4 T_d	North Windham, Maine, USA	Alexander 1989‡
chromite No.1†	$Fe_{0.4}Mg_{0.7}Cr_{1.4}Al_{0.5}O_4$		4	Black Lake, Megantic Co, Québec	
chromite No.2†	$Fe_{0.4}Mg_{0.7}Cr_{1.4}Al_{0.5}O_4$		4	Sverdlovsk area, Ural, Russia	
hercynite No.1†§	$FeAl_2O_4$§		4	Unknown locality	Hill 1984 Harrison et al. 1998
hercynite No.2†	$Fe_{0.7}Mg_{0.3}Al_2O_4$‖		4	Ronsberg, Bohemia, Czech Rep.	
grandidierite	$(Mg,Fe)Al_3(BO_4)(SiO_4)O$	1.1	5 C_{3v}	Marotrana, Madagascar	Stephenson and Moore 1969 Seifert and Olesch 1977 Farges 2001
fayalite	Fe_2SiO_4		6 O_h	Allevard, Isère, France	Lager and Meagher 1978 Princivalle and Secco 1985
olivine	$(Mg_{0.9}Fe_{0.1})_2SiO_4$	9.6	6	San Carlos, Arizona, USA	
edenite	$NaCa_2Mg_5AlSi_7O_{22}(OH)_2$		6	Russel, New York, USA	Makino and Tomita 1989
cummingtonite	$(Mg, Fe)_7Si_8O_{22}(OH)_2$		6	La Paz County, Arizona, USA	Yang and Smith 1996
wüstite†	FeO		6	synthetic	Yamamoto 1982
periclase†	$Fe_{0.1}Mg_{0.9}O$		6	synthetic	Waychumas et al. 1994
enstatite	$Mg_{1.7}Fe_{0.3}Si_2O_6$		6	Unknown locality, India	Ghose et al. 1989 Zhang et al. 1997
diopside	$CaMg_{0.9}Fe_{0.1}Si_2O_6$	3.6	6	Mugui, Esperito Sancto, Brazil	Garbonin et al. 1989 White 1966
siderite	$FeCO_3$		6	Nova Lima, Minas Gerais, Brazil	Reeder 1983 Gil et al. 1992
Fe(II)-sulfate	$FeSO_4·7H_2O$		6	Synthetic, Merk Inc. 99.0%	
hedenbergite	$CaFeSi_2O_6$		6	Phakuwa, Sankhuwa Sabha, Nepal	Maslenikov 1979
almandine#	$Ca_{0.3}Fe_{1.5}Mg_{1.2}Al_2Si_3O_{12}$		8	Gore Mtn, New York, USA	Ambruster et al. 1992
perovskite-type	$Mg_{0.88}Fe_{0.12}SiO_3$		8+4	synthetic	Farges et al. 1993

* Unweathered.
† A small amount of 6-coordinated Fe^{3+} may be present in these samples.
‡ also see Hawthorne et al. 1994, Henderson et al. 1997, and Koch-Muller et al. 1998.
§ Slightly inverse, with 5% at most of Fe^{2+} in the octahedral site.
‖ About 20% inverse.
$Alm_{49}Pyr_{39}Spe_1Gro_{11}$.

TABLE 1b. Model compounds for Fe^{3+}

Sample	Chemical formula	wt% Fe_2O_3	CN symmetry	Origin	References
ferriorthoclase	$Fe:KAlSi_3O_8$		4 T_d	Itrongay, Madagascar	Faye 1969 White et al. 1986
Fe-berlinite*	$Fe_{0.01}Al_{0.99}PO_4$		4	synthetic	Eschahed and Bonneviot pers. Commun.
	$Fe:LiAlO_2$		4	synthetic	Waychunas and Rossman 1983
	$FePO_4$		4	synthetic	Arnold et al. 1982
yoderite	$(Mg,Al,Fe)_8Si_4(O,OH)_{20}$	6.1	5 C_{3v}	Mautia Hill, Kongwa, Tanzania	Fleet et al. 1962 Higgins et al. 1982
aegirine	$NaFeSi_2O_6$		6 O_h	Eker, Norway	Cameron et al. 1973
andradite	$Ca_3Fe_{1.8}Al_{0.2}Si_3O_{12}$		6	unknown locality, Arizona	—
mélanite	$Ca_3(Fe,Ti)_2Si_3O_{12}$		6	unknown locality, Sonora, Mexico	—
Fe(III)-sulfate	$Fe_2(SO_4)_3 · 2H_2O$		6	synthetic, Merk Inc. 99.9%	—
epidote	$Ca_2(Fe,Al)_3(SiO_4)_3(OH)$		6	Green Monster Mtn, Alaska, USA	—
ferrihydrite	$FeOOH$		6	synthetic	—
goethite	$FeOOH$		6	synthetic	—
hematite	$\alpha\text{-}Fe_2O_3$		6	synthetic	—

* A small amount of 6-coordinated Fe^{3+} may be present in these samples.

compounds with low Fe concentrations (such as enstatite, grandidierite, etc.), XAFS spectra were collected in the fluorescence mode with the sample positioned 45° with respect to the beam. The fluorescence yield was measured as a function of X-ray energy using a pin-diode detector. A MnO filter (3 μ absorbance) before the fluorescence detector was used to minimize unwanted elastic scattering. XANES spectra were collected from ~50 eV below to 200 eV above the Fe K-edge (7050–7300 eV), with 0.1 eV steps for the pre-edge region (7108–7116 eV). Some spectra presented here (as indicated in subsequent tables) were recorded at the Stanford Synchrotron Radiation Laboratory (SSRL), USA on wiggler beamline IV-1 using a Si (220) monochromator (energy resolution (FWHM) of ~1.6 eV at the Fe K edge for a beam height of ~1 mm). The SPEAR storage ring operating conditions were 3 GeV electron energy and 30–100 mA electron current. The fluorescence yield was measured using a Stern-Heald-type detector (Lytle et al. 1984) with Xe in the fluorescence detector ion chamber. A MnO

filter (3 μ absorbance) and Ag-soller slits were used to minimize unwanted elastic scattering and filter fluorescence, respectively. To remove the high-energy harmonics from the incident X-ray beam, the monochromator was detuned reducing the intensity of the incoming beam by 40%.

The XANES spectra were normalized in absorbance by fitting the spectral region from 7050 to 7090 eV (the region before the pre-edge) using a Victoreen function and subtracting this as background absorption (see Fig. 1). The spectra were then normalized for atomic absorption, based on the average absorption coefficient of the spectral region from 7200 to 7300 eV (i.e., after the edge crest: Fig. 1). To extract the pre-edge feature the contribution of the edge jump to the pre-edge was modeled using a spline function that was used to interpolate the background using the data several eV before and after the pre-edge feature (Fig. 1). The pre-edges were deconvoluted into pseudo-Voigt components using the software PeakFit4 to derive normalized height, position, half-width, and integrated

intensity (Table 2). As a first step, the pseudo-Voigt components were allowed to vary in shape (i.e., with variable amount of Gaussian versus Lorentzian peak shapes). Most pre-edge models converged to a Gaussian fraction of between 20% and 60%, with an average of 49%. The pre-edges were then deconvoluted a second time, by fixing the Gaussian fraction to 50%. Also, the pseudo-Voigt functions were modeled assuming the same width for each pre-edge feature. The average width of pre-edge features for all model compounds is ~1.4 eV. This parameter was constrained to minimize the number of correlated parameters, as the number of independent data points in the pre-edge features is relatively small. No more than three peaks were fit in the experimental spectra (except for hematite where five peaks were fit), as suggested by the analysis of the second derivative of the spectra as well as a core-hole

deconvolution analysis (see Kosarev 1990 and Farges et al. unpublished manuscript). The "average" pre-edge information was derived by calculating the "integrated intensity" (sum of the integrated intensities of each component) and its centroid (intensity-weighted average of the components' positions).

RESULTS

Ferrous model compounds

Figure 2 shows the normalized XANES spectra collected at the Fe K-edge for the various model compounds investigated in this study. The pre-edge feature can be observed in all spectra near 7113 eV. The normalized pre-edge features and their deconvolutions into 50:50 pseudo-Voigt components are shown in Figure 3 for selected model compounds (the deconvoluted data are in Table 2a).

TABLE 2a. Pre-edge characteristics for Fe^{2+} model compounds

Sample	Height*	Component Position (eV)	Width (eV)	Area	Total area	Centroid (eV)	R^2
gillespite	0.0126	7111.70	1.331	0.0202	0.0363	7112.29	0.9978
	0.0100	7113.02	1.331	0.0161			
staurolite	0.1001	7111.56	1.451	0.1756	0.2441	7111.98	0.9989
	0.0392	7113.05	1.451	0.0685			
hercynite No.1	0.0951	7111.52	1.479	0.1700	0.2558	7112.02	0.9985
	0.0482	7113.02	1.479	0.0858			
hercynite No. 2	0.0737	7111.50	1.540	0.1362	0.2095	7112.02	0.999006
	0.0398	7112.99		0.0733			
chromite No.1	0.0702	7111.62	1.383	0.1176	0.1812	7112.11	0.9984
	0.0381	7113.01	1.383	0.0636			
chromite No. 2	0.0590	7111.42	1.380	0.0988	0.1570	7111.97	0.9976
	0.0347	7112.90	1.380	0.0582			
grandidierite	0.0410	7111.56	1.474	0.0731	0.1288	7112.38	0.9996
	0.0266	7113.26	1.474	0.0473			
	0.0048	7114.49	1.474	0.0084			
fayalite	0.0194	7111.22	1.631	0.0385	0.1025	7112.04	0.9983
	0.0158	7111.81	1.631	0.0313			
	0.0164	7113.24	1.631	0.0327			
olivine†	0.0137	7111.22	1.363	0.0219	0.0461	7111.89	0.9987
	0.0084	7111.99	1.363	0.0142			
	0.0064	7113.23	1.363	0.0100			
enstatite†	0.0137	7111.18	1.202	0.0201	0.0598	7112.04	0.9986
	0.0146	7112.04	1.202	0.0215			
	0.0124	7112.88	1.202	0.0182			
diopside	0.0130	7111.15	1.264	0.0199	0.0513	7112.06	0.9988
	0.0110	7112.05	1.264	0.0169			
	0.0095	7113.31	1.264	0.0145			
hedenbergite	0.0180	7111.25	1.279	0.0279	0.0722	7112.09	0.9991
	0.0158	7112.09	1.279	0.0245			
	0.0128	7113.29	1.279	0.0198			
wüstite	0.0167	7111.46	1.442	0.0291	0.0834	7112.45	0.9988
	0.0135	7112.48	1.442	0.0234			
	0.0178	7113.37	1.442	0.0309			
periclase	0.0077	7111.57	1.059	0.0099	0.0228	7112.40	0.9856
	0.0052	7112.53	1.059	0.0068			
	0.0047	7113.60	1.059	0.0061			
$FeSO_4 \cdot 7H_2O$	0.0132	7111.28	1.254	0.0202	0.0448	7112.16	0.9979
	0.0077	7112.20	1.254	0.0118			
	0.0083	7113.51	1.254	0.0128			
siderite	0.0115	7111.39	1.229	0.0172	0.0370	7112.16	0.9988
	0.0074	7112.26	1.229	0.0110			
	0.0059	7113.56	1.229	0.0088			
cummingtonite	0.0161	7111.20	1.166	0.0222	0.0698	7112.02	0.9987
	0.0182	7112.01	1.166	0.0253			
	0.0160	7112.84	1.166	0.0223			
edenite	0.0171	7111.18	1.287	0.0268	0.0623	7111.98	0.9990
	0.0114	7111.97	1.287	0.0180			
	0.0111	7113.20	1.287	0.0175			
almandine	0.0202	7111.73	1.420	0.0346	0.0463	7112.17	0.9981
	0.0069	7113.47	1.420	0.0117			
$(Mg,Fe)SiO_3$	0.0288	7111.62	1.961	0.0696	0.1079	7112.11	0.9961
	0.0159	7112.99	1.961	0.0383			

* Normalized height.
† Spectra measured at SSRL.

TABLE 2b. Pre-edge characteristics for Fe^{3+} model compounds

Sample	Component				Total area	Centroid	R^2
	Height*	Position (eV)	Width (eV)	Area		(eV)	
$FePO_4$	0.1727	7113.55	1.642	0.3423	0.3423	7113.55	0.9988
$Fe:LiAlO_2$	0.1805	7113.44	1.546	0.3351	0.3351	7113.44	0.9970
Fe-berlinite	0.1409	7113.60	1.561	0.2677	0.2677	7113.60	0.9982
Fe-orthoclase	0.1868	7113.44	1.504	0.0232	0.3577	7113.44	0.9993
yoderite	0.0865	7113.26	1.628	0.1691	0.1911	7113.43	0.9993
	0.0102	7114.70	1.628	0.0220			
aegirine†	0.0228	7112.72	1.619	0.0425	0.10020	7113.51	0.9997
	0.0310	7114.10	1.619	0.0577			
andradite	0.0244	7112.78	1.344	0.0400	0.0757	7113.48	0.9994
	0.0218	7114.26	1.344	0.0357			
melanite	0.0236	7112.75	1.383	0.0399	0.0759	7113.46	0.9990
	0.0214	7114.25	1.383	0.0360			
$Fe_2(SO_4)_3\cdot 2H_2O$	0.0224	7112.93	1.415	0.0387	0.0722	7113.61	0.9970
	0.0194	7114.40	1.415	0.0335			
epidote	0.0177	7112.67	1.548	0.0333	0.0643	7113.56	0.9986
	0.0237‡	7113.49‡	1.548‡	0.0447‡			
	0.0165	7114.51	1.548	0.0310			
ferrihydrite	0.0301	7112.97	1.571	0.0580	0.1193	7113.47	0.9993
	0.0318	7113.94	1.571	0.0613			
	0.0082‡	7115.6‡	2.875‡	0.0250‡			
goethite	0.0209	7112.72	1.326	0.0341	0.0889	7113.58	0.9997
	0.0335	7114.12	1.326	0.0548			
	0.0089‡	7115.56‡	1.599‡	0.0152‡			
	0.0069‡	7117.03‡	1.657‡	0.0121‡			
hematite	0.0300	7112.68	1.322	0.0489	0.1236	7113.47	0.9998
	0.0458	7113.98	1.322	0.0747			
	0.0247‡	7115.22‡	1.666‡	0.0468‡			
	0.0191‡	7116.68‡	1.624‡	0.0332‡			
	0.0069‡	7117.83‡	1.474‡	0.0109‡			

* Normalized height.
† Spectra measured at SSRL.
‡ These pre-edge components result from processes other than a 1s→3d transition (probably involving Fe 2nd neighbors). Their width and shape have been allowed to vary independently in the fitting process from the pre-edge components related to the 1s→3d/4p transition. Their shapes always converged to a pure Gaussian contribution, suggesting a possible Fe-O-Fe multiple-scattering origin.

When Fe^{2+} is 4-coordinated (square planar and tetrahedral), the pre-edge can be fit satisfactorily with two components, centered near 7111.6(1) and 7113.1(1) eV, respectively (Table 2a). However, crystal-field theory predicts four transitions for 4-coordinated environments (see Westre et al. 1997; Arrio et al. 2000). The two additional transitions could not be fit in a statistically robust way because their height is relatively low and the spectral difference may be beyond the core-hole resolution limit. Slight differences were observed in the two hercynites examined in this study, with the second sample (hercynite no. 2) having a pre-edge intensity slightly lower than the first one (these differences were also observed in their XANES spectra: Fig. 2a). These spectral differences are related to some degree of inversion (i.e., the presence of some Fe^{2+} in the octahedral site) in the structure of the hercynite no. 2 sample.

For 5-coordinated Fe^{2+} (as in grandidierite), a third component could be fit, centered near 7114.6(3) eV. This extra peak can be assigned to the presence of Fe^{3+} in the same crystallographic site as Fe^{2+} (Farges 2001). This explains also why the centroid for this compound at 7112.4(1) eV is slightly above the average centroid position for Fe^{2+} model compounds at 7112.1(1) eV.

For 6-coordinated Fe^{2+} model compounds, all spectra must be fit with three components, in agreement with theoretical predictions (Westre et al. 1997; Arrio et al. 2000). When the octahedron of O atoms is regular around Fe^{2+} (as in siderite or

Fe^{2+} sulfate), the three predicted features are observed directly in the raw pre-edge data. However, with increasing site distortion, only two maxima are distinguishable in the pre-edge spectra. However, three components are required to model such pre-edges. The centroids for siderite and wüstite show the largest deviation (±0.3 eV) from the average value of 7112.1 eV, despite the fact that the energy calibration was double checked. We can not exclude some contribution arising from Fe^{3+} in our wüstite sample, which would shift the centroid toward higher energy. In these oxides, divalent Fe is known to be randomly substituted in the cation sublattice, with a cation vacancy associated with two trivalent iron ions resulting in an average redox state of Fe close to 2.11 (Waychunas 1983; Hilbrandt and Martin 1999; Rosenfeld and Holstein 1999). The intensity of the pre-edge is inversely correlated with the extent of centrosymmetry of the crystallographic site of Fe. For enstatite, the integrated intensity of the pre-edge feature is relatively high for 6-coordinated Fe^{2+}, in agreement with Fe being preferentially located in the very distorted M2-sites (Closmann et al. 1996; Huang et al. 2000). In contrast, the pre-edge for olivine is lower than that for fayalite and enstatite, confirming that Fe partitions favorably to the less distorted M1 sites in Mg-rich olivine (Burns 1974).

When Fe^{2+} is 8- (almandine-rich garnet) or 12-coordinated [$(Mg,Fe)SiO_3$ perovskite], two maxima and two fitted compo-
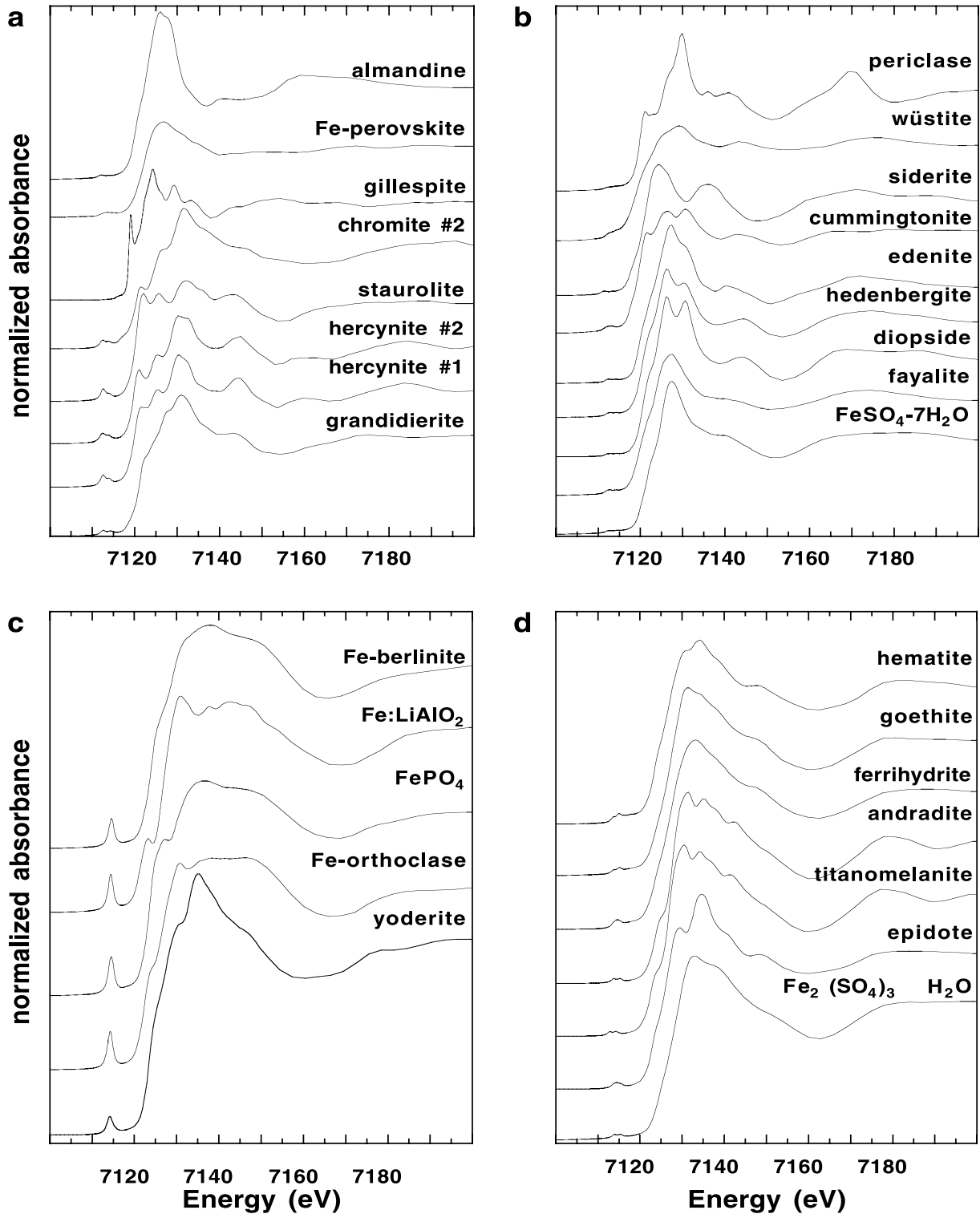
FIGURE 2. Selected Fe K-edge XANES spectra for the model compounds investigated in this study: (**a**) Fe^{2+} in 4, 5, and 8-coordinated sites; (**b**) Fe^{2+} in 6-coordinated sites; (**c**) Fe^{3+} in 4- and 5-coordinated sites; (**d**) Fe^{3+} in 6-coordinated sites.
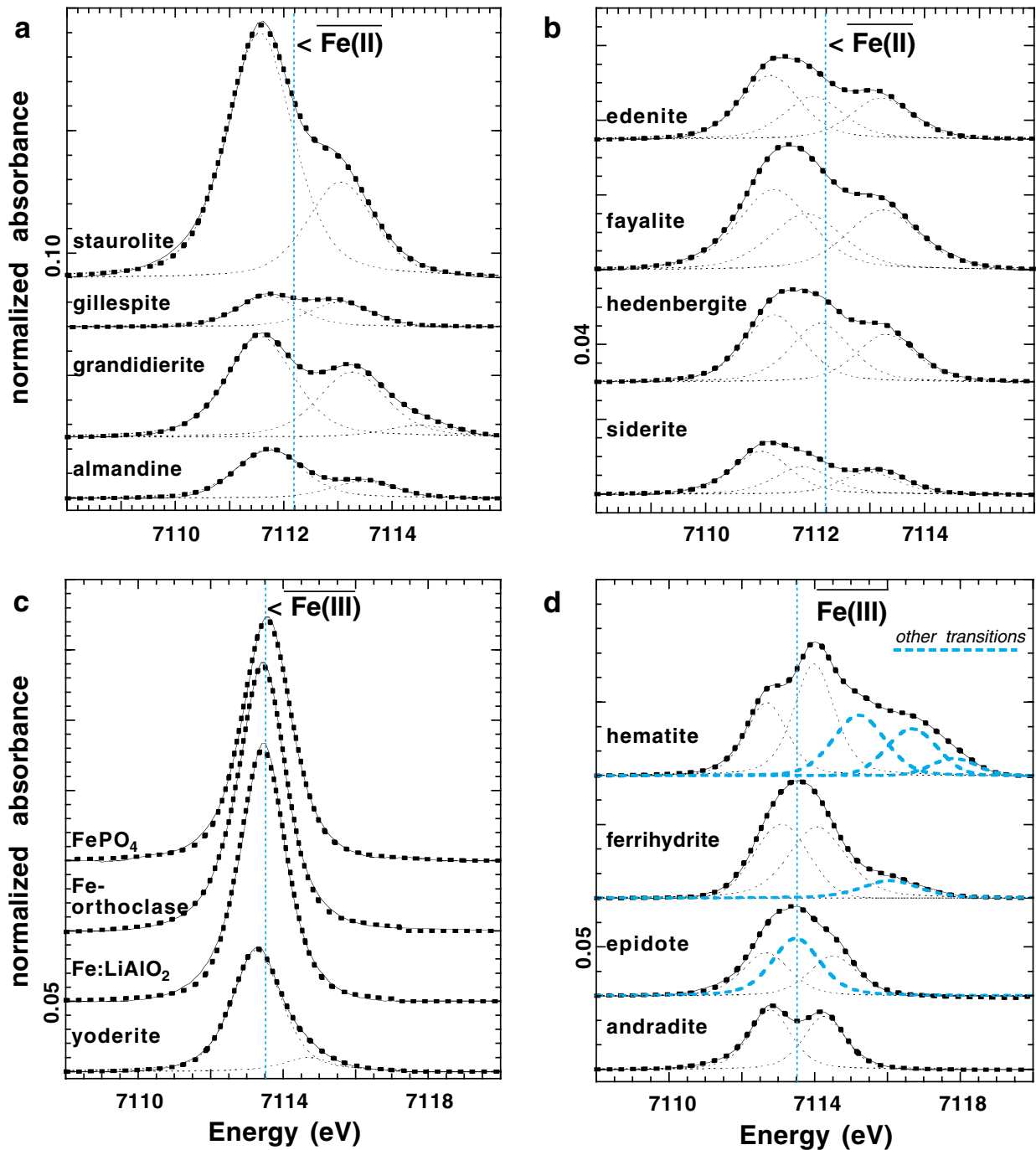
FIGURE 3. Selected normalized pre-edge spectra (Fe K-edge) and the best model calculated (using PeakFit4); (**a**) pre-edges for 4-, 5-, and 8-coordinated Fe^{2+} model compounds showing mostly two contributions; (**b**) pre-edges for 6-coordinated Fe^{2+} model compounds showing three contributions; (**c**) pre-edges for 4- and 5-coordinated Fe^{3+} model compounds showing mostly one contribution; (**d**) pre-edges for 6-coordinated Fe^{3+} model compounds showing two contributions relevant to the $1s \rightarrow 3d/4p$ transition (black dotted lines) and extra transitions (in gray dotted lines) related to some Fe clustering (epidote, ferrihydrite, and hematite).

nents are observed in the pre-edge spectra. For all Fe^{2+}-bearing model compounds, the average centroid of the pre-edge is near 7112.1(1) eV, but the intensity of the pre-edge (i.e., the integrated intensity for all peaks) varies from 0.022(3) (Fe-periclase) to up to 0.2258(10) (hercynite no. 1).

Ferric model compounds

For the Fe^{3+} model compounds, the same trends seen in the Fe^{2+} model compounds are observed, but with some differences. The centroid of these pre-edges is located near 7113.5(1) eV (Table 2b). The most intense pre-edges (~0.3) are observed for

the most non-centrosymmetric geometry (tetrahedral). Only one significant component could be fit for these pre-edges, despite the fact that theoretical predictions suggest the presence of two transitions (see Westre et al. 1997 and Arrio et al. 2000). However, the second transition is very low in intensity, making its contribution too poorly resolved to be modeled robustly.

The pre-edge intensity decreases to 0.19 for yoderite, in which Fe^{3+} is 5-coordinated in a trigonal bipyramid. In yoderite, one dominant component is observed in its pre-edge feature. But a shoulder near 7115 eV was detected, which could be due to a trace amount of octahedrally coordinated Fe^{3+}. The lack of theoretical calculations for this geometry does not permit a comparison with theoretical predictions.

For octahedrally coordinated Fe^{3+}, the pre-edge intensity decreases to 0.12. When the octahedron of O atoms around Fe^{3+} is slightly distorted (as in andradite, aegirine and Fe^{3+} sulfate), two components are observed in the pre-edge spectra, in agreement with theoretical predictions, and can be fit with centroids near ~7112.8 and ~7114.3 eV. In Fe-oxides and hydroxides (ferrihydrite, goethite, and hematite), one to three extra components are observed in the pre-edge spectra above 7115 eV. These contributions, which are not predicted by theory (two components for high spin, O_h-symmetry Fe^{3+}-bearing compounds), have different shapes as compared to the other lines: they converged to quasi-Gaussian shape (instead of pseudo-Voigt 50:50) and their width is often slightly larger (~1.6 eV instead of ~1.4 eV). Also, their intensity increases clearly with the degree of $Fe(O,OH)_6$-octahedral polymerization (ferrihydrite > goethite > hematite). Polarization-dependent XAFS experiments suggest that these contributions in hematite are related to long-range order around Fe, involving 3d orbitals of distant iron neighbors (Dräger et al. 1988). Therefore, we excluded these contributions in calculating the pre-edge centroid and total integrated intensity. In this case, the pre-edge parameters are much more in agreement with those of the other Fe^{3+} model compounds, including those for ferrihydrite (for which an anomalously high pre-edge intensity was erroneously thought to be related to the presence of tetrahedrally coordinated Fe^{3+} by Manceau and Gates (1997). The same arguments can be applied to epidote, which shows three maxima and three fitted features centered near 7112.7, 7113.5, and 7114.5(1) eV (Table 2b). In comparison with all model compounds in which Fe^{3+} is 6-coordinated (O_h), and based on theoretical calculations (Westre et al. 1997; Arrio et al. 2000), the second feature (at 7113.5 eV) cannot be related to a $1s \rightarrow$ 3d or 4d transition. This contribution was therefore excluded from the calculation of the pre-edge parameters (the origin of this extra line remains unknown but may be related to the clustering of Fe in this structure, as observed previously for iron oxyhydroxides: Wu et al. 1996).

DISCUSSION

Redox state of Fe

Examination of the pre-edge parameters for all model compounds (Table 2) suggests that the energy positions of the maxima of the pre-edge for Fe^{2+} and Fe^{3+} compounds are sepa-

rated by ~2.1 eV, in agreement with past studies (Waychunas et al. 1983; Bajt et al. 1994; Galoisy et al. 2001). However, the pre-edge parameters most reliable for extracting information are the pre-edge peak centroid and total integrated intensity, excluding pre-edge components that are not predicted by theoretical calculations. The centroid is most sensitive to oxidation state, confirming the observations of Bajt et al. (1994). The pre-edge intensity is confirmed to be most sensitive to site centrosymmetry (see also Waychunas et al. 1983) with the most centrosymmetric Fe coordinations having the lowest intensity. This parameter alone, however, can not be used to derive quantitative coordination information (for example, the pre-edge intensity for gillespite, which contains square planar Fe^{2+}, is about the same as for almandine). The two main components observed for $^{IV}Fe^{2+}$ ([Ar]3d^6; T_d symmetry) correspond mainly to dipolar electronic transitions to the 3d crystal-field split (e and t_2) levels. Similarly, the first two peaks of the pre-edges for Fe in sites with O_h symmetry (near 7111 and 7112 eV) are related to quadrupolar electronic transitions to the t_{2g} levels (the third feature at 7113.4 eV is related to transitions to e_g levels: Dräger et al. 1988; Westre et al. 1997; Heumann et al. 1997). Similar conclusions can be reached for Fe^{3+} ([Ar]3d^5), but under T_d symmetry only one transition is dipole allowed (two transitions are allowed for O_h symmetry) (Westre et al. 1997). Pre-edges for 5-coordinated Fe^{2+} and Fe^{3+} are related to dipole transitions, due to the lack of centrosymmetry in that geometry (C_{3v} symmetry). The splitting of the pre-edge feature decreases with lower Fe^{2+}-coordination, and from Fe^{2+} to Fe^{3+}, in agreement with crystal-field theory wherein Δq (T_d) ~ $^4/_9$ Δq (O_h), see Burns (1993).

When the most common coordination environments of Fe are considered (excluding the square planar geometry and those environments having an Fe-coordination number above 6), there is an indirect correlation between pre-edge integrated intensity and Fe-coordination. In contrast, there is no clear variation in pre-edge position with coordination, as observed previously for Ti^{4+} and Ni^{2+} (Farges et al. 1996; Farges et al. unpublished manuscript). Heumann et al. (1997) confirmed that the Fermi level is located just below the split 3d/4p crystal field levels of Fe, whereas, for Ni^{2+}, it is located in between the split 3d/4p levels. Then, the observable final states of Ni^{2+} (t_2 and e_g for T_d and O_h symmetry, respectively) in the K-edge XANES spectrum cannot be located at the same energy for octahedral and tetrahedral Ni-coordinations. This is related to the crystal field energy level splitting Δq, which decreases with decreasing Ni-coordination. For Fe in contrast, all 3d states can be observed so the centroids of their energy levels correspond to the free ion energy (when located in a spherical potential), which is roughly constant with coordination.

The respective centroids for Fe^{2+} and Fe^{3+} are separated by 1.4(1) eV (Fig. 4) in agreement with the findings of Galoisy et al. (2001) who reported a 1.5 eV separation. Because of these differences in centroid position between Fe^{2+} and Fe^{3+}, it is potentially possible to derive redox information from the Fe K-pre-edge position. However, because pre-edge position can vary non-linearly with oxidation state (see the case of Ti: Farges et al. 1996), a systematic investigation of the variation of pre-
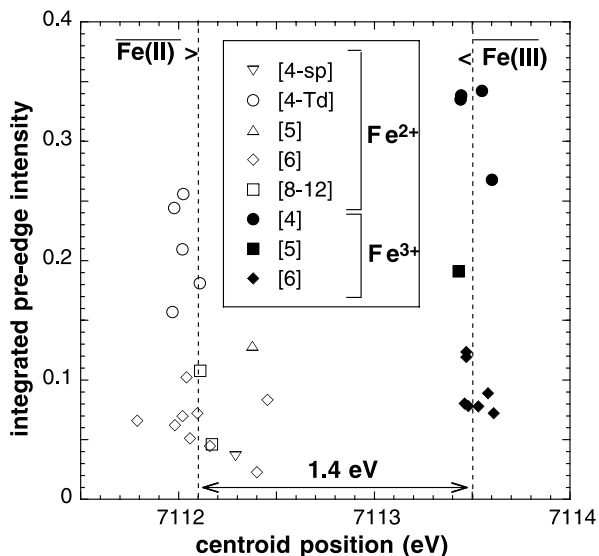
FIGURE 4. Summary of pre-edge information, showing the separation between Fe^{2+} and Fe^{3+} centroids. The relatively large deviation for grandidierite (up-pointing triangles), gillespite (down-pointing triangles), and Fe^{2+}-oxides may be due to some minor amounts of Fe^{3+} in these samples, despite the fact that no contribution arising from Fe^{3+} iron could be resolved. The standard errors of the pre-edge intensities (from the least-squares fits of the pre-edge) are of the order of ±0.001 (see Table 2), whereas the precision for the measurements of pre-edge energy positions is ±0.05eV, based on the reproducibility of monochromator positions within multiple measurements.

edge position for mixtures of Fe^{2+} and Fe^{3+} is required, and variations in site geometry must be considered.

Effect of mixtures of Fe^{2+} and Fe^{3+} on the Fe K-pre-edge feature

To examine the effect of mixed valence state, we collected Fe K-edge XANES spectra for the six possible mixtures of four phases (staurolite, siderite, $FePO_4$ and hematite) containing $^{IV}Fe^{2+}$, $^{VI}Fe^{2+}$, $^{IV}Fe^{3+}$, and $^{VI}Fe^{3+}$. Mixtures were prepared on a molar basis with respect to only the Fe atoms in the compounds. This was done to simulate the variation of the pre-edge with variation of redox state and/or structural site as it may occur in solid solutions of minerals. Such a simulation might not be absolutely exact when applied to real solid solutions of the same structural sites considered here. However, deviations should be minor as pre-edge transitions are related to crystal field splitting and are not observed to be affected by changes in medium and long-range structure (for instance, the pre-edges for siderite and wüstite or andradite and Fe^{3+}-sulfate are respectively identical). We compare the measured pre-edge spectra of these mixtures with those derived from calculated linear combinations of the normalized XANES spectra of the respective end-members in Figure 5. The pre-edges in Figure 5 were extracted from the mixed XANES spectra, using the procedure described in the experimental section.

The calculated pre-edge spectrum for a 50:50 mixture (in mol% Fe) of staurolite and siderite compares well with that measured experimentally (Fig. 5a), suggesting that the calculated pre-edges are representative of the experimental ones. The experimental spectrum for the mixture between $FePO_4$ and hematite compares well with the calculated 50:50 spectrum at higher energies but shows slightly higher intensities at the peak maximum (Fig. 5b). These differences must be related to the differences in the background of the pre-edge of the experimental and calculated spectrum, which are not suppressed by the background-subtraction procedure. The experimental spectrum of the staurolite-$FePO_4$ mixture (Fig. 5c) compares well with the calculated 40:60 spectrum which comes close to the actual mixture of the sample used in the experiment. For the mixture between hematite and siderite (Fig. 5d) differences between experimental and calculated 50:50 mixture are greater but still both spectra are close to each other. The experimental spectrum of the staurolite-hematite mixture matches well the calculated 30:70 mixture at the low energy limb but considerably drops off below on the high energy limb (Fig. 5e). This, in parallel to the $FePO_4$-Hematite join (Fig. 5b), must be related to differences in the background of both spectra. Comparison of the experimental and calculated 50:50 mixture of the siderite-$FePO_4$ join reveals only slight differences (Fig. 5f).

Deviations found between experimental and calculated spectra occur when the background in the pre-edge region changes considerably from one end-member to the other. These background changes arise from the shift of the main-edge position due to different redox states of the two end-members and from those spectral features in the pre-edge region which are not related to $1s \rightarrow 3d/4d$ transition (in mixtures containing hematite). Hence the strongest effect can be observed for the join staurolite-hematite (Fig. 5e).

These variations are summarized in the refined pre-edge information of Figure 6. We have created this plot by calculating the mixtures from the average values of the centroid for Fe^{2+} and Fe^{3+} and the average integrated intensity of the four end-member cases, respectively: Fe^{2+}/Fe^{3+}, tetrahedral/octahedral iron. We observed that the extraction of the parameters from each mixture shown in Figure 5 amplifies the effects of the pre-edge background on the resulting pre-edge parameters. Alternatively, the use of average values minimizes these effects and thus, gives a more generalized view on the variation of the pre-edge. Examination of Fig. 6 suggests that the variation of the pre-edge parameters is linear at a constant redox state ($^{IV}Fe^{2+}/^{VI}Fe^{2+}$ join). The same observation is true for the mixture between $^{IV}Fe^{3+}$ and $^{VI}Fe^{3+}$, provided that the extra transitions in hematite above 7115 eV are not taken into account (not related to a $1s \rightarrow 3d/4d$ transitions). Variations with redox state at a constant coordination number (4- and 6-coordinations, respectively) appear less linear. The most non-linear variations in both centroid and intensity are observed when both, the oxidation state and the coordination number of Fe vary simultaneously. This non-linear variation of the increments across the joins arises from the mixing of pre-edges with strongly differing intensities and therefore, is found to be strongest for $^{VI}Fe^{2+}/^{IV}Fe^{3+}$ join.

normalized absorbance

Energy (eV)
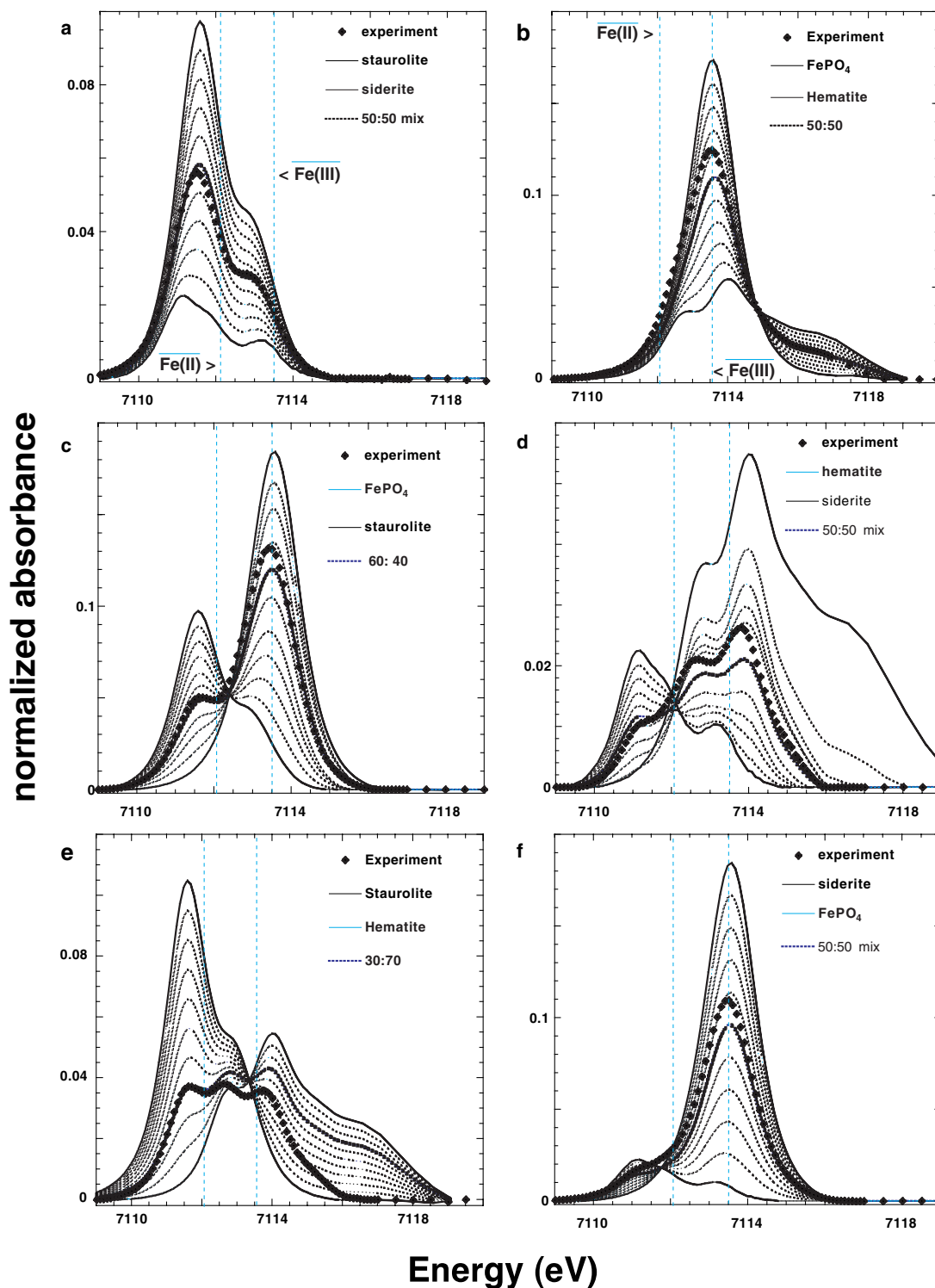
FIGURE 5. Normalized pre-edges for the 6 joins of mixtures; (**a**) staurolite plus siderite (the oxidation state is constant and Fe²⁺), compared to an experimental spectrum for a 50:50 mixture of both (all mixtures are in terms of mol% Fe); (**b**) same for FePO₄ and hematite (constant Fe³⁺ redox); (**c**) FePO₄ plus staurolite (constant low coordination), compared to an experimental spectrum for a 40:60 mixture of both; (**d**) siderite plus hematite (constant high coordination), compared to an experimental spectrum for a 50:50 mixture; (**e**) staurolite plus siderite (oxidation state and coordination are variable), compared to an experimental spectrum for a 30:70 mixture of both; (**f**) siderite plus FePO₄ (oxidation state and coordination are variable), as compared to an experimental spectrum for a 50:50 mixture of both. For further discussion, see text.
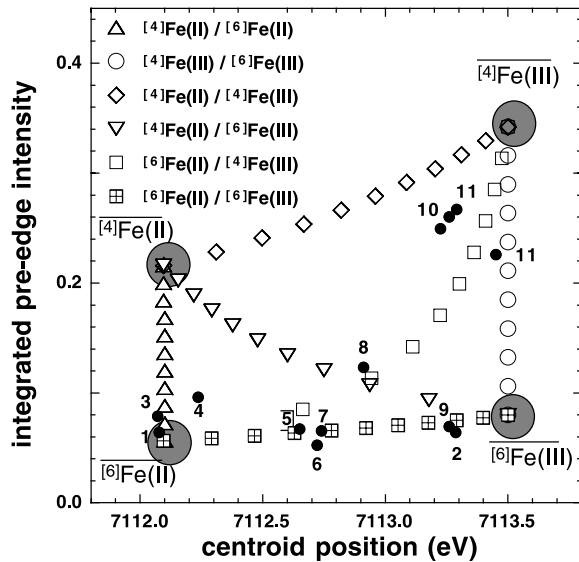
FIGURE 6. Summary of pre-edge characteristics for the binary mixtures between $^{IV}Fe^{2+}$, $^{VI}Fe^{2+}$, $^{IV}Fe^{3+}$, and $^{VI}Fe^{3+}$. In addition, pre-edge information for Fe in example minerals is plotted. Note that this diagram does not consider the possibility of 5-coordinated Fe^{2+}/Fe^{3+} environments, as well as more complex mixtures (such as ternaries,). The standard errors of the pre-edge intensities (from the least-squares fits of the pre-edge) are of the order of ±0.001 (see Table 2), whereas the precision level of the measurements of pre-edge energy positions is ±0.05eV, based on the reproducibility of multiple measurements. Black circles are 1 humite; 2 rhodonite no. 1; 3 rhodonite no. 2; 4 dumortierite; 5 potassian kaersutite; 6 kaersutite; 7 vesuvianite no. 1; 8 vesuvianite no. 2; 9 franklinite, 10 magnetite no. 1 & no. 2; 11 labradorite; 12 maghemite.

FIGURE 7. Variation of centroid position with redox ratio of the mixtures. This plot shows the considerable non-linearity in joins where both redox state and coordination geometry change. Dashed line represents the "half-way energy position."

Determination of the redox state of Fe by XAFS: strengths and limitations

By analyzing Figure 6, a rough estimate of the Fe redox state can be obtained by considering the centroid of the pre-edge position, as previously pointed out by Bajt et al. (1994). In Figure 7 the variation of the centroid of the four mixtures with changing redox state is plotted versus the bulk redox state of the mixture. This plot highlights the considerably non-linear variation of the centroid when redox state and coordination vary at the same time. None of the 50:50 mixtures plots at the energy position located approximately "halfway" between the end members for Fe^{2+} and Fe^{3+} (dashed line in Fig. 7), mixtures of the $^{VI}Fe^{2+}/^{VI}Fe^{3+}$ and $^{IV}Fe^{2+}/^{IV}Fe^{3+}$ joins being the closest. Thus, a more accurate estimation of the redox state of Fe must take into account the coordination chemistry of Fe, especially close to the end-members. Also, the analysis of the shape of the pre-edge is a useful indicator of the possible end-members involved in the unknown sample. When a single component is observed in the pre-edge, this is a strong indication of the presence of some tetrahedrally coordinated Fe^{3+}. When this "single component" has a shoulder at lower energies, this is evidence for Fe^{2+} (whereas a shoulder on the high-energy side is an indication of the presence of 6-coordinated Fe^{3+}). When the shoulder

on the low energy side, also has a relatively strong intensity, this provides some evidence for tetrahedrally coordinated Fe^{2+} (and so on). However, some pre-edges are not unique in shape. For instance, when a weak contribution near 7112.0 eV can be detected, it may be due to major amounts of 6-coordinated Fe^{2+} or to minor amounts of tetrahedrally coordinated Fe^{2+}. Also, the possibility of 5-coordinated Fe^{2+} was not considered in these mixtures: mixtures of 4- and 5-coorinated Fe and of 5- and 6-coordinated Fe should show variations "halfway" between that of tetrahedrally and octahedrally coordinated iron.

XANES analysis of Fe-oxidation state: a case study on a few Fe-bearing minerals

Magnetite. Table 3 describes a series of minerals in which the oxidation state of Fe atoms was determined using the methods presented here. We first apply these methods to two unweathered magnetites, which show similar XANES (Fig. 8a) and pre-edge features (Fig. 8b). Analysis of the pre-edge features for these magnetites (Table 4) shows that three components contribute to the pre-edge as follows: a main contribution near 7113.0-7113.1(1) eV and two shoulders near 7111.6 and 7114.4(1) eV (these values are the averages of the pre-edge characteristics for the two magnetites derived from the fits). The main component arises dominantly from tetrahedrally coordinated Fe^{3+}, whereas the shoulders arise from Fe^{2+} (but its coordination—theoretically 6—could not be estimated accurately from the spectra) and octahedrally coordinated Fe^{3+}, respectively.

The pre-edge position for magnetite (either the maximum or the centroid) indicates a mixture of Fe^{2+} and Fe^{3+}, although it is relatively close to that for $^{IV}Fe^{3+}$. This result is consistent with lower resolution pre-edge characteristics extracted for

TABLE 3. Samples used as example minerals for evaluating their Fe^{3+}/SFe ratio

Sample	Chemical formula	aspect, color	Origin
magnetite no.1	($Fe^{3+}Fe^{2+}Fe^{3+}O_4$)	octahedral, black	unknown loc., California, U.S.A.
magnetite no.2	($Fe^{3+}Fe^{2+}Fe^{3+}O_4$)	octahedral, black	Pfitschal, Tyrol, Austria
maghemite	γ-Fe_2O_3	brown	synthetic (BASF tape)
franklinite	~ (Zn,Mn^{2+},Fe^{2+}) $(Fe^{3+},Mn^{3+})_2O_4$	massive, red	Franklin, New Jersey, U.S.A.
dumortierite	$(Al, Fe)_{6.5-7}(BO_3)$ $(SiO_4)_3(O,OH)_3$	massive, blue	Ambatalahinanahary, Sahirina, Madagascar
kaersutite	~ $NaCa_2((Fe,Mg)_4Ti)Si_6Al_2O_{22}(OH)_2$	phenocrystal black	unknown locality, U.S.A.
potassian kaersutite	$K_{0.6}Na_{0.4}Ca_{1.8}[Mg_{2.9}Fe_{1.1}Al_{0.4}Ti_{0.6}]$	phenocrystal black	Moussenat (?) Haute-Loire, France
$Si_{5.8}Al_{2.2}O_{22}(OH)_2$			
cordierite	$(Mg,Fe)_2Al_4Si_5O_{18}$	massive, dark blueish	Bamble, Norway
vesuvianite #1	Fe: $Ca_{10}Mg_2Al_4(SiO_4)_5$	brown-green	Sierra de Las Cruces, Mexico
vesuvianite #2	$(Si_2O_7)_2(OH)_4$	gemmy, yellow	Coahuila, Mexico
labradorite	Fe:$(Na, Ca)AlSi_3O_8$*	gemmy, yellowish	Los Lamentos Chihuahua, Mexico
humite	$(Mg,Fe^{2+})_7(SiO_4)_3(F,OH)_2$†	red-brown	Tilly Foster, New York, U.S.A.
rhodonite no.1	$(Mn,Fe)SiO_3$	massive, pink weathered	Sverdlovsk, Ural Mountains, Russia
rhodonite no.2	$Mn_{0.7}Fe_{0.2}Ca_{0.01}SiO_3$	gemmy, red	Broken Hill, New South Wales, Australia

* ~0.5 wt% FeO.
† 1.7 wt% FeO.
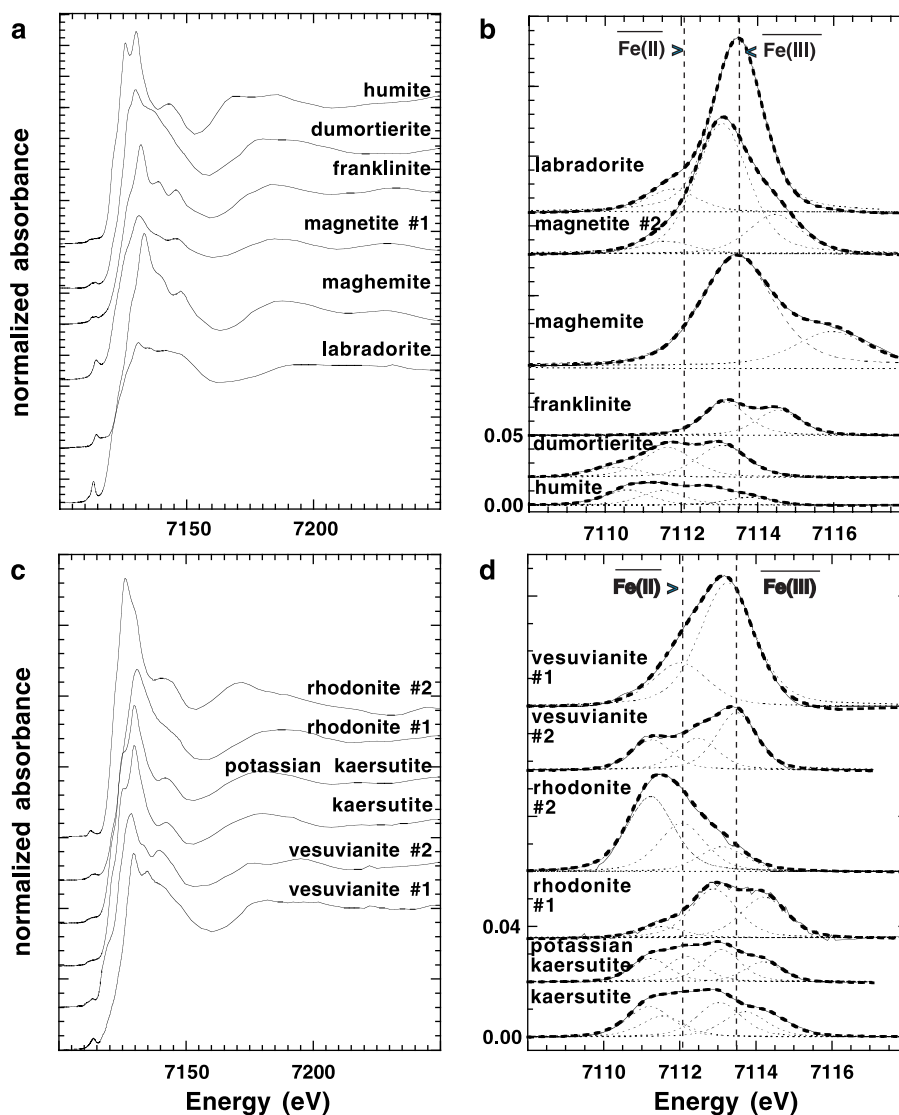
FIGURE 8. Fe K-edge XANES (**a,c**) and pre-edge spectra (**b,d**) for the "unknown" minerals used to evaluate their Fe oxidation states; (**a**) note that the spectrum of humite is similar to those for some of the inosilicates and the three spinels (franklinite, magnetite no. 1 and magnetite no. 2); (**b**) note the large differences between franklinite and magnetite no. 2, due to the presence of tetrahedrally coordinated Fe^{3+} iron in the latter sample; (**c**) note the large differences in the XANES spectra for the rhodonites and vesuvianites, whereas the amphiboles (potassian kaersutite and kaersutite) are rather similar; (**d**) note again the large differences in the pre-edge spectra for the rhodonites and vesuvianites, suggesting large redox and structural variations among the samples studied.

TABLE 4. Pre-edge information of the example minerals

Sample	Component				Total area	Centroïd	R^2
	Height*	Position (eV)	Width (eV)	area (eV)			
magnetite no.1	0.0084	7111.64	1.7638	0.0177	0.2496	7113.21	0.9985
	0.0830	7113.00	1.7638	0.1765			
	0.0261	7114.40	1.7638	0.0554			
magnetite no.2	0.0094	7111.62	1.6159	0.0186	0.2602	7113.25	0.9993
	0.0931	7113.06	1.6159	0.1847			
	0.0287	7114.42	1.6159	0.0569			
maghemite‡	0.0791	7113.45	2.2512	0.2259	0.2259	7113.45	0.9992
	0.0244‡	7115.94‡	2.2512‡	0.0699‡			
franklinite	0.0241	7112.65	1.3504	0.0397	0.0696	7113.25	0.9989
	0.0181	7114.05	1.3504	0.0299			
dumortierite	0.0072	7110.29	1.5318	0.0135	0.0962	7112.09	0.9977
	0.0214	7111.64	1.5318	0.0399			
	0.0229	7113.07	1.5318	0.0428			
kaersutite	0.0111	7111.20	1.3672	0.0184	0.0673	7112.56	0.9983
	0.0091	7112.13	1.3672	0.0153			
	0.0126	7113.04	1.3672	0.0210			
	0.0076	7114.28	1.3672	0.0126			
potassian	0.0085	7111.23	1.1772	0.0122	0.0527	7112.64	0.9988
kaersutite	0.0092	7112.15	1.1772	0.0133			
	0.0117	7113.10	1.1772	0.0168			
	0.0073	7114.19	1.1772	0.0104			
cordierite†	0.0093	7111.26	1.260	0.0144	0.0336	7112.02	0.9975
	0.0065	7112.05	1.260	0.0100			
	0.0060	7113.18	1.260	0.0092			
vesuvianite no.1	0.0109	7111.25	1.2527	0.0165	0.0657	7112.66	0.9963
	0.0115	7112.47	1.2527	0.0175			
	0.0209	7113.49	1.2527	0.0317			
vesuvianite no. 2	0.0164	7112.02	1.6922	0.0333	0.1236	7112.91	0.9963
	0.0444	7113.24	1.6922	0.0903			
labradorite	0.0165	7111.75	1.5564	0.0310	0.2672	7113.29	0.9995
	0.1262	7113.49	1.5564	0.2362			
humite	0.0110	7110.60	1.3882	0.0185	0.0641	7111.91	0.9991
	0.0105	7111.50	1.3882	0.0177			
	0.0111	7112.68	1.3882	0.0186			
	0.0056	7113.77	1.3882	0.0093			
rhodonite no.1	0.0041	7111.54	1.4107	0.0071	0.0642	7112.87	0.9888
	0.0179	7112.90	1.4107	0.0312			
	0.0149	7113.21	1.4107	0.0259			
rhodonite no. 2	0.0305	7111.44	1.1081	0.0396	0.0721	7112.07	0.9408
	0.0189	7112.58	1.1081	0.0246			
	0.0061	7113.65	1.1081	0.0079			

* Normalized height.
† Spectra measured at SSRL.
‡ These pre-edge components result from processes other than a 1s→3d transition (probably involving Fe 2nd neighbors) see also Table 2 and text.

other unweathered magnetite samples in an earlier study (Bajt et al. 1994). Therefore, there is no resolution effect on the pre-edge position of magnetite (see Galoisy et al. 2001). In contrast, this shift in energy can be related to the presence of both Fe^{2+} and Fe^{3+} in magnetite, which is consistent with the correlation between the centroid of the pre-edge position and the $Fe^{3+}/\Sigma Fe$ ratio (Bajt et al. 1994).

The pre-edge parameters of magnetite plot near the binary join between octahedrally coordinated Fe^{2+} and tetrahedrally coordinated Fe^{3+} (Fig. 6); for this sample, the redox state of Fe is estimated to be 65% Fe^{3+} and 35% Fe^{2+}. This result is in agreement with the inverse nature of magnetite [Fe_3O_4 has 1/3 of the total Fe as $^{VI}Fe^{2+}$ (B-Site), 1/3 as $^{IV}Fe^{3+}$ (A-site), and 1/3 as $^{VI}Fe^{3+}$ (B-site)]. On the other hand, the actual oxidation state and coordination number of Fe in magnetite cannot be extrapolated from the $^{VI}Fe^{2+}/^{IV}Fe^{3+}$ join, as we have clear evidence for three components ($^{VI}Fe^{2+}$, $^{IV}Fe^{3+}$, and $^{VI}Fe^{3+}$) in the pre-edge spectrum. The proximity of the pre-edge parameters for the two magnetites of this study to the $^{VI}Fe^{2+}/^{IV}Fe^{3+}$ join is, then, fortuitous (despite the fact that the estimate of oxidation state appears correct). On the other hand, we calculated that the parameters of a ternary mixture of $^{VI}Fe^{2+}$, $^{IV}Fe^{3+}$, and $^{VI}Fe^{3+}$ would plot below the $^{VI}Fe^{2+}/^{IV}Fe^{3+}$ join. Hence, the observed position of the magnetites would suggest the presence of $^{IV}Fe^{2+}$ in these magnetite samples. It is known that $^{IV}Fe^{2+}$ can be found in the magnetite structure in presence of Ti or Cr (e.g., Lindsley 1976). However, these two compounds are found only to a small extent in these samples (EMPA analyses showed Ti: <1000 ppm, Cr_2O_3: <3 wt%), which may be too small to cause the observed anomaly. However, it was also shown by measurements on pure magnetite at high temperature that Fe^{2+} is distributed over both tetrahedral and octahedral sites, reaching random distribution at about 1450 °C (Wu and Mason 1981). Theoretically, magnetite should be completely inverse at room temperature, however, the distribution found at room temperature can be dependent on the thermal history of the sample and may reflect distributions stable a higher temperature (Wu and Mason 1981; Faller and Birchenall 1970). By extrapolation of their measurements at high temperature Wu and Mason (1981) predict a low amount of $^{IV}Fe^{2+}$ at room temperature which is in agreement

with room-temperature site distributions found by magnetic moment measurements by Pauthenet (1952). However, the pre-edge suggests a higher amount of $^{IV}Fe^{2+}$ than found in those studies (<3% in tetrahedral A-site). Hence, we suggest that the observed low amounts of Ti and Cr in these natural samples may stabilize $^{IV}Fe^{2+}$ at a higher level.

Maghemite. Maghemite (γ-Fe_2O_3) may be considered as a fully oxidized magnetite with 1/3 of the Fe sites being vacant, thus a mixture of $^{IV}Fe^{3+}$ and $^{VI}Fe^{3+}$ (e.g., Weber and Hafner 1971). Similar to hematite, the pre-edge shows an extra transition on its high-energy limb, which is too high in energy position to be assigned to a $1s \rightarrow 3d/4d$ transition. When considering only the low energy transitions, the pre-edge information plots on the $^{IV}Fe^{3+}/^{VI}Fe^{3+}$ join, with a $^{IV}Fe^{3+}/\Sigma Fe$ ratio of 0.6. This is consistent with the crystal chemistry and with statistical distribution of the vacancies over both Fe sites (Weber and Hafner 1971).

Franklinite. This spinel (see de Grave et al. 1996) shows a pre-edge similar to that of andradite, but its centroid is slightly shifted towards lower energy (by ~0.3 eV). In Figure 6, the pre-edge parameters for this franklinite [Zn, Mn^{2+}, Fe^{3+}, $(Fe^{2+},Mn^{3+})_2O_4$– 60.0 wt% Fe_2O_3] are located close to the $^{VI}Fe^{3+}$ end-member, on the $^{VI}Fe^{2+}/^{VI}Fe^{3+}$ join (but the $^{IV}Fe^{2+}/^{VI}Fe^{3+}$ join cannot be excluded). Therefore, we conclude that ~90% of the iron is Fe^{3+} in this sample. This result is in excellent agreement with a recent systematic crystal structure study of several franklinites from this locality (Lucchesi et al. 1999). However, we can not determine the coordination number for Fe^{2+} in this sample, due to its relatively low contribution as compared to Fe^{3+}.

Labradorite, humite, dumortierite, amphiboles, and cordierite. The Fe-bearing labradorite ($An_{60}Ab_{40}$, ca. 0.5 wt% FeO) has a pre-edge feature close to that for ferri-orthoclase, but some contribution from Fe^{2+} is observed. Based on Figure 6, the pre-edge parameters for labradorite are close to the $^{VI}Fe^{2+}/^{IV}Fe^{3+}$ join, suggesting that 80% of the Fe is Fe^{3+} in that sample, in agreement with other Fe^{2+}/Fe^{3+} determinations by optical and electron paramagnetic resonance (EPR) spectroscopies (Hofmeister and Rossman 1984). The position of the labradorite data point to the left of the $^{VI}Fe^{2+}/^{IV}Fe^{3+}$ join suggests a distribution of Fe^{2+} in both, tetrahedral and octahedral sites. Hofmeister and Rossman (1984) assigned their spectroscopic observations on terrestrial plagioclase to Fe^{2+} being distributed in two distorted octahedral sites. On the other hand, observations by Behrens et al. (1990) and Longhi et al. (1976) indicate that Fe^{2+} is mostly found on the tetrahedral site in natural and synthetic plagioclase. The observed pre-edge may indicate that both assignments for the site of Fe^{2+} are valid. However, a more comprehensive analysis, which includes theoretical calculations of the complete XANES region is needed to interpret the observed XANES.

Humite and dumortierite have XANES spectra (Fig. 8a) and pre Fe^{2+}-edge parameters (Fig. 8b, Table 4) typical of octahedrally coordinated Fe^{2+}, which is consistent with their crystal structure (Ribbe and Gibbs 1971; Robinson et al. 1973; Moore and Araki 1978; Alexander et al. 1986). The slightly shifted pre-edge of this dumortierite from Madagascar may be related to the presence of trace amounts of Fe^{3+} (~5 at%, based on Fig.

4). Its total Fe concentration is 2000 ppm, which makes an absolute Fe^{3+} concentration of less than 100 ppm in that sample. The blue color of dumortierite is related to Fe^{2+}- Fe^{3+} charge transfer (Alexander et al. 1986). The same conclusion was reached for grandiderite (Farges 2001), a mineral often associated with dumortierite in Madagascar.

The two amphiboles, potassian kaersutite and kaersutite, show quite similar XANES (Fig. 8c) and pre-edge spectra, the latter spectra can be modeled by considering two contributions from Fe^{2+} and Fe^{3+}, respectively (Fig. 8d), both in octahedral sites. The $Fe^{3+}/\Sigma Fe$ ratio determined by pre-edge analysis in these two amphiboles (0.6 and 0.7, respectively) is consistent with EMPA analysis of the Fe redox (0.6 for both samples) using the method of Fialin et al. (2000) which includes matrix corrections for amphiboles. In addition, redox determinations by Mössbauer spectroscopy on these samples (collected at both 77 and 293 K) resulted in a $Fe^{3+}/\Sigma Fe$ ratio of 0.62 ± 0.03 for the potassian kaersutite and 0.69 ± 0.03 for the kaersutite sample, as well, supporting the determination by pre-edge analysis.

The pre-edge of the (low) cordierite from Bamble, Norway, suggests the presence of Fe^{2+} in a relatively regular 6-coordinated environment (Table 4). There is no evidence for tetrahedrally coordinated Fe in this sample, in contrast to observations on other natural cordierites reported by Geiger et al. (2000).

Rhodonite. More variable results were observed for the rhodonites investigated. Their Fe K-XANES and pre-edge spectra (Figs. 8c and 8d) are quite different. The gemmy-, translucent and dark red rhodonite (no. 2) from Broken Hill, Australia (12.6 wt% FeO) has mostly Fe^{2+} (>90% octahedrally coordinated). This result is in agreement with crystal-field and Mössbauer information derived for other samples of rhodonite from this locality (Dickson 1975). In contrast, rhodonite no. 1 (pink and weathered from the Ural Mountains) is rich in Fe^{3+} (80% based on Fig. 6). Their pre-edge spectra are typical of octahedral iron, in agreement with their crystal structure (Narita et al. 1977) and the preference of Fe to enter distorted octahedral sites (Dickson 1975). The presence of Fe in both oxidation states is similar to the case for Mn, which is also present in this mineral as divalent (major) and trivalent (minor amount) Mn (see Moore and Threadgold 1981). No evidence for the presence of 5- or 7-coordinated Fe^{2+} was found in any of these samples (the contributions are probably hidden by the stronger contribution arising from iron in 6-coordinated sites).

Vesuvianite. The Fe-oxidation states and coordination numbers are also different for the two vesuvianite samples investigated as suggested by the XANES and pre-edge spectra (Figs. 8c and 8d). In vesuvianite, Fe can be located in two sites with quite different coordination environments: ^VFe (square pyramidal geometry, Fe^{2+} or Fe^{3+}, ~2/3 of the total Fe) and $^{VI}Fe^{3+}$ (~1/3 of the total Fe) (Valley et al. 1985; Ohkawa et al. 1992). In the two samples investigated from Mexico, the pre-edge features show two contributions arising from both Fe^{2+} and Fe^{3+}. In Figure 6, vesuvianite no. 1 is located on the $^{VI}Fe^{2+}/^{VI}Fe^{3+}$ join (close to the 40:60% point). Its pre-edge parameters are not consistent with the presence of some $^VFe^{2+}$ (the pre-edge intensity is too low). In contrast, the second vesuvianite is located on the $^{IV}Fe^{2+}/^{VI}Fe^{3+}$ join [close to the point with 80% of Fe as $^{VI}Fe^{3+}$]. However, these pre-edge parameters may also be con-

sistent with some Fe^{2+} present in a 5-coordinated site (see Osborne and Burns 1978; Ohkawa et al. 1992) as the join between $^{V}Fe^{2+}$ and $^{VI}Fe^{3+}$ can be drawn slightly below that for $^{IV}Fe^{2+}/^{VI}Fe^{3+}$. Given the position in Figure 6 found for this sample, the $^{VI}Fe^{2+}/^{IV}Fe^{3+}$ join might also be relevant. However, because of the crystallographic constraints cited above, we may exclude this possibility.

General applicability of the technique

Analysis of the pre-edge spectra of Fe in model compounds and mixtures shows that it is possible to derive iron redox information from the centroid of the pre-edge position. Estimation of the $Fe^{3+}/\Sigma Fe$ ratio is more accurate when the influence of Fe-coordination on both the centroid and the total pre-edge intensity is considered. However, estimation of the $Fe^{3+}/\Sigma Fe$ ratio is more precise when crystal chemical information about Fe is also considered in deriving information about the redox state of Fe in an "unknown" crystalline sample from iron pre-edge information. This is especially important in phases where the Fe^{3+} and Fe^{2+} are localized in different site geometries. In most rock-forming minerals, however, Fe is often octahedrally coordinated (Fe^{2+} or Fe^{3+}), and there is a quasi-linear variation of the pre-edge position with the redox of Fe, which allows a rather accurate determination of valence and structural information in agreement with studies by Bajt et al. (1994) and Delaney et al. (1996). Therefore, estimation of the Fe-redox state by XANES spectroscopy in minerals such as biotite and amphibole (where Fe is mostly 6-coordinated) done in-situ in rock thin sections provides a desirable possibility to correct thermobarometers for metamorphic processes which are based on knowledge of the true Fe^{2+} content in these minerals.

When studying redox and speciation of Fe in glasses using XAFS methods (Galoisy et al. 2001; Wilke et al. 1999) or, in-situ, at the glass/melt transition (Wilke et al. unpublished data), strong variation in the coordination chemistry of Fe is possible as Fe might be distributed over (at least) 4 distinct site geometries (Brown et al. 1995) or a continuum of sites ranging from 4-coordinated to 5-, and 6-coordinated Fe^{2+} (Rossano et al. 2000). This makes the analysis of the pre-edge much more challenging, and a careful examination of the pre-edge features is required, which requires a very high signal-to-noise ratio, the best experimental resolution possible, and the use of appropriate model compounds and data analysis methods. The application of these methods to the in-situ determination of the redox state and coordination environment of Fe in melts at ambient or high-pressure conditions as well as in hydrothermal systems or in vacuum sensitive materials (hydrous contaminated soils or biotic materials) are potential applications of these methods.

REFERENCES CITED

Alexander, V.D. (1989) Iron distribution in staurolite at room and low temperatures. American Mineralogist, 74, 610–619.

Alexander, V.D., Griffen, D.T., and Martin, T.J. (1986) Crystal chemistry of some Fe- and Ti-poor dumortierites. American Mineralogist, 71, 786–794.

Armbruster, T., Geiger, C.A., and Lager, G.A (1992) Single-crystal X-ray structure study of synthetic pyrope almandine garnets at 100 and 293 K. American Mineralogist, 77, 512–521.

Arnold, H., Brueggemann, W., and Muellner, M. (1982) Strukturen von AlPO₄—Cristobalit und-Pseudocristobalit sowie von FePO₄ -Berlinit. Zeitschrift für Kristallographie, 159, 10–11.

Arrio, M.A., Rossano, S., Brouder, Ch., Galoisy, L., and Calas, G. (2000) Calculation of multipole transitions at the Fe K pre-edge through p-d hybridization in the Ligand Field Multiplet model. Europhysics Letters, 51 454–460.

Bajt, S., Sutton, S.R., and Delaney, J.S. (1994) X-ray microprobe analysis of iron redox states in silicates and oxides using X-ray absorption near edge structure (XANES). Geochimica et Cosmochimica Acta, 58, 5209–5214.

Behrens, H., Johannes, W., and Schmalzried, H. (1990) On the mechanism of cation diffusion processes in ternary feldspars. Physics and Chemistry of Minerals, 17, 62–78.

Brown, G.E. Jr., Farges, F., and Calas, G. (1995) X-ray scattering and X-ray spectroscopy studies of silicate melts. In J.F. Stebbins, D.B. Dingwell, and P.F. McMillan, Eds., Structure, Dynamics, and Properties of Silicate Melts, vol. 32, p. 317–410. Reviews in Mineralogy, Mineralogical Society of America, Washington, D.C.

Burns, R.G. (1974) The polarized spectra of iron in silicates: Olivine; A Discussion of neglected contributions from Fe^{2+} ions in M(1) Sites. American Mineralogist, 59, 625–629.

——(1993) Mineralogical Applications of Crystal Field Theory, 551 p. Cambridge University Press, Cambridge, U.K.

Cameron, M., Sueno, S., Prewitt, C.T., and Papike, J.J (1973) High-temperature crystal chemistry of acmite, diopside, hedenbergite, jadeite, spodumene, and ureyite. American Mineralogist, 58, 594–618.

Carbonin, S., Salviulo, G., Munno, R., Desiderio, M., and Dal-Negro, A. (1989) Crystal-chemical examination of natural diopsides; some geometrical indications of Si-Ti tetrahedral substitution. Mineralogy and Petrology, 41, 1–10.

Closmann, C. Knittle, E., and Bridges, F. (1996) An XAFS study of the crystal chemistry of Fe in orthopyroxene. American Mineralogist, 81, 1321–1331

Cressey, G., Henderson, C.M.B., and van der Laan, G. (1993) Use of L-edge X-ray absorption spectroscopy to characterize multiple valence states of 3d transition metals; a new probe for mineralogical and geochemical research. Physics and Chemistry of Minerals, 20, 111–119.

De Grave, E., Vochten, R., and Vandenberghe, R.E. (1996) A Mössbauer effect study of franklinite from Sterling Hill, New Jersey. In M. Darby Dyar, Ed., Mineral spectroscopy; a tribute to Roger G. Burns: Geochemical Society Special Publication Vol. 5, p. 105–116.

Delaney, J.S., Bajt, S., Newville, M., Sutton, S.R., and Dyar, M.D. (1996a) Measurement of Fe oxidation state and coordination in geological glasses by synchrotron microXANES spectroscopy. American Geophysical Union 1996 Fall Meeting in San Francisco, CA. 77, 835–836. American Geophysical Union, Washington, D.C.

Delaney, J.S, Bajt, S., Sutton, S.R., and Dyar, M.D. (1996b) In situ microanalysis of $Fe^{3+}/?Fe$ ratios in amphibole by X-ray absorption near edge structure (XANES) spectroscopy. In M.D. Dyar, C.A. McCammon, and M.W. Schaefer, Eds., Mineral Spectroscopy: A tribute to Roger Burns: Geochemical Society Special Publication 5, 289–304.

Delaney, J.S., Dyar, M.D., Sutton, S.R., and Bajt S. (1998) Redox ratios with relevant resolution; solving an old problem by using the synchrotron microXANES probe. Geology, 26, 139–142

Dickson, B.L. (1975) The iron distribution in rhodonite. American Mineralogist, 60, 98–104.

Dräger, G., Frahm, R., Materlik, G., and Brummer, O. (1988) On the multipole character of the X-ray transitions in the pre-edge structure of Fe K absorption spectra. Physica Status Solidi B, 146, 287–293.

Dunlap, R.A., Edelman, D.A., and Mackay, G.R. (1998) A Mössbauer effect investigation of correlated hyperfine parameters in natural glasses (tektites). Journal of Non-Crystalline Solids, 223, 141–146.

Dyar, M.D. (1985) A review of Mössbauer data on inorganic glasses: the effects of composition on iron valency and coordination. American Mineralogist, 70, 304–

316.

Dyar, M.D., Delaney J.S., Sutton, S.R., and Schaefer M.W. (1998) Fe³⁺ distribution in oxidized olivine: A synchrotron micro-XANES study. American Mineralogist, 83, 1361–1365.

Faller, J.G. and Birchenall, C.E. (1970) The temperature dependence of ordering in magnesium ferrite. Journal of Applied Crystallography, 3, 496–503.

Farges F. (2001) Crystal chemistry of iron in natural grandidierites: a XAFS spectroscopy study at the Fe K-edge. Physics and Chemistry of Minerals (2001).

Farges, F., Guyot, F., Andrault, D., and Wang, Y. (1993) Local environment around Fe in Mg₀.₉Fe₀.₁SiO₃ perovskite. An Fe K-edge XAS study. European Journal of Mineralogy, 6, 303–312.

Farges, F., Brown, G.E., Jr., and Rehr, J.J. (1996) Coordination chemistry of Ti(IV) in silicate glasses and melts. I. XAFS study of Ti coordination in oxide model compounds. Geochimica et Cosmochimica Acta, 60, 3023–3038.

Faye, G.H. (1969) The optical absorption spectrum of tetrahedrally bonded Fe³⁺ in orthoclase. Canadian Mineralogist, 10, 112–117.

Fialin, M., Wagner, C., and Humler, E. (2000) Direct determination of Fe²⁺- Fe³⁺ concentrations with the electron microprobe. Journal of Conference Abstracts, 5(2), 400.

Fleet, S.G. (1962) The crystal structure of yoderite. Acta Crystallographica, 15, 721–728.

Galoisy, L., Calas, G., and Arrio, M.A. (2001) High-resolution XANES spectra of iron in minerals and glasses: structural information from the pre-edge. Chemical Geology, 174, 307–319.

Garvie, L.A.J. and Busek, P. (1998) Ratios of Fe²⁺ to Fe³⁺ iron from nanometer-sized areas in minerals. Nature, 396, 667–670.

Gauthier, C., Solé, V.A., Signorato, R., Goulon, J., and Moguiline, E. (1999) The ESRF beamline ID26: X-ray absorption on ultra dilute sample. Journal of Synchrotron Radiation, 6, 164–166.

Geiger, C.A., Armbruster, T., Khomenko, V., and Quartieri, S. (2000) Cordierite I: The coordination of Fe²⁺. Journal of Conference Abstracts, 5, 40.

Ghose, S., Schomaker, V., and McMullan, R.K. (1986) Enstatite; a neutron diffraction refinement of the crystal structure and a rigid-body analysis of the thermal vibration. Zeitschrift für Kristallographie, 176, 159–175.

Gil, P.P., Pesquera, A., and Velasco, F. (1992) X-ray diffraction, infrared and Mössbauer studies of Fe-rich carbonates. European Journal of Mineralogy, 4, 521–526.

Harrison, R.J., Redfern, S.A.T., and O'Neill, H.St. C. (1998) The temperature dependence of the cation distribution in synthetic hercynite (FeAl₂O₄) from in-situ neutron structure refinements. American Mineralogist, 83, 1092–1099.

Hawthorne, F.C., Oberti, R., Ungaretti, L., Caucia, F., and Callegari, A. (1994) Crystal-structure refinement of hydrogen-rich staurolite. Canadian Mineralogist, 32, 491–495.

Heald, S.M., Amonette, J.E., Turner, G.D., and Scott, A.D. (1995) An XAFS study of the oxidation of structural iron in biotite mica by solutions containing Br₂ or H₂O₂. Physica B, 208–209, 604–606.

Henderson, C.M.B., Charnock, J.M., Cressey, G., and Griffen, D.T. (1997) An EXAFS study of the local structural environments of Fe, Co, Zn and Mg in natural and synthetic staurolites. Mineralogical Magazine, 408, 613–624.

Heumann, D., Dräger, G., and Bocharov S. (1997) Angular-dependance in the K pre-edge XANES of cubic crystals: the separation of the empty metal e_g and t_2g states of NiO and FeO. Journal de Physique IV France, 7 C2, 481–483.

Higgins, J.B., Ribbe, P.H., and Nakajima, Y. (1982) An ordering model for the commensurate antiphase structure of yoderite. American Mineralogist, 67, 76–84.

Hilbrandt, N. and Martin, M. (1999) A quantitative in situ Fe K-XAFS study (T>1270 K) on the oxidation degree of iron in (Mg₁₋ₓFeₓ)₁₋ᵧO. Journal of Synchrotron Radiation, 6, 489–491.

Hill, R.J. (1984) X-ray powder diffraction profile refinement of synthetic hercynite American Mineralogist, 69, 937–942.

Huang, E., Chen, C.H., Huang, T., Lin, E.H., and Xu, Ji-an (2000) Raman spectroscopic characteristics of Mg-Fe-Ca pyroxenes. American Mineralogist, 85, 473–479

Hofmeister, A.M. and Rossman, G.R. (1984) Determination of Fe³⁺ and Fe²⁺ concentrations in feldspar by optical absorption and EPR spectroscopy. Physics and Chemistry of Minerals, 11, 213–224.

Koch-Mueller, M., Kahlenberg, V., Bubenick, W., and Gottschalk, M. (1998) Crystal-structure refinement of synthetic Fe- and Mg-staurolite by Rietveld analysis of X-ray powder-diffraction data. European Journal of Mineralogy, 10, 453–460.

Kosarev, E.L. (1990) Shannon's super resolution limit for signal recovery. Inverse Problems, 6, 55–76.

Krause, M.O. and Oliver, J.H. (1979) Natural widths of atomic K and L levels, K alpha X-ray lines and several KLL auger lines. Journal of Physical and Chemical Reference Data 8, 329–338.

Lager, G.A. and Meagher, E.P. (1978) High-temperature structural study of six olivines. American Mineralogist, 63, 365–377.

Lindsley, D.H. (1976) The crystal chemistry and structure of oxide minerals as exemplified by the Fe-Ti oxides. Mineralogical Society of America, Short Course Notes, 3, 1–52.

Longhi, J., Walker, D., and Hays, J.F. (1976) Fe and Mg in plagioclase. Geochimica Cosmochimica Acta Suppl., 7, 1281–1300.

Lucchesi, S., Russo, U., and Della Giusta, A. (1999) Cation distribution in natural Zn-spinels; franklinite. European Journal of Mineralogy, 11, 501–511.

Lytle, F.W., Greegor, R.B., Sandstrom, D.R., Marques, D.R., Wong, J., Spiro, C.L., Huffman, G.P., and Huggins, F.E. (1984) Measurement of soft X-ray absorption spectra with a fluorescence ion chamber detector. Nuclear Instruments and Methods in Physics Research Section A, 226, 542–548.

McCammon, C.A. (1997) Perovskite as a possible sink for Fe³⁺ iron in the lower mantle. Nature, 387, 694–696.

Makino, K. and Tomita, K. (1989) Cation distribution in the octahedral sites of hornblendes. American Mineralogist, 74, 1097–1105.

Manceau, A. and Gates, W.P. (1997) Surface model for ferrihydrite. Clays and Clay Minerals, 45, 448–460.

Maslenikov, A.V. (1979) Structure refinement for natural hedenbergite. International Geology Review, 21, 877–879.

Moore, P.B. and Araki, T. (1978) Dumortierite, Si₃B[Al₆.₇₅Si₀.₂₅O₁₇.₂₅(OH)₀.₇₅]; a detailed structure analysis. Neues Jahrbuch für Mineralogie Abhandlungen, 132, 231–241.

Moore, F.H. and Threadgold, I.M. (1981) The iron distribution in rhodonite; a neutron diffraction study. International Congress of Crystallography, 12, C–189.

Mysen, B.O. (1991) Relations between structure, redox equilibria of iron, and properties of magmatic liquids. In Perchuk LL, Kushiro I, Eds., Advances in Physical Chemistry, 9, 41–98.

Narita, H., Koto, K., and Morimoto, N. (1977) The crystal structures of the MnSiO₃ 3D polymorphs (rhodonite- and pyroxmangite-type). Mineralogical Journal, 8, 329–342.

Newville, M., Sutton, S., Rivers, M., and Eng, P. (1998) Micro-beam X-ray absorption and fluorescence spectroscopies at GSECARS: APS beamline 13ID. Journal of Synchrotron Radiation, 6, 353–355.

Ohkawa, M., Yoshiasa, A., and Takeno, S. (1992) Crystal chemistry of vesuvianite; site preferences of square-pyramidal coordinated sites. American Mineralogist, 77, 945–953.

Osborne, M. and Burns, R.G. (1978) Crystal chemistry, optical properties and Moessbauer spectroscopy of vesuvianite; significance of five-coordinated iron sites. Abstracts with Programs, Geological Society of America, 7, 466.

Pabst, A. (1959) Structures of some tetragonal sheet silicates. Acta Crystallographica, 12, 733–739.

Parkinson, I.J. and Arculus, R.J. (1997) The redox state of subduction zones; insights from arc-peridotites. Chemical Geology, 160, 409–423.

Pauthenet, R. (1952) Spontaneous magnetization of ferrites. Annales de Physique (Paris),7, 710–747.

Pettifer, R.F. and Hermes, C. (1985) Absolute energy calibration of X-ray radiation from synchrotron sources. Journal of Applied Crystallography, 18, 404–412.

Princivalle, F. and Secco, L. (1985) Crystal structure refinement of 13 olivines in the forsterite-fayalite series from volcanic rocks and ultramafic nodules. Tschermaks Mineralogische und Petrographische Mitteilungen, 34, 105–115.

Reeder, R.J. (1983) Crystal chemistry of the rhombohedral carbonates. In R.J. Reeder, Ed., Carbonates; mineralogy and chemistry, p. 1–47. Reviews in Mineralogy, Mineralogical Society of America, Washington, D.C.

Ribbe, P.H. and Gibbs, G.V. (1971) Crystal structures of the humite minerals; III, Mg/Fe ordering in humite and its relation to other ferromagnesian silicates. American Mineralogist, 56, 1155–1173.

Robinson, K., Gibbs, G.V., and Ribbe, P.H. (1973) Crystal structures of the humite minerals: IV, clinohumite and titanoclinohumite. American Mineralogist, 58, 43–49 (see also the correction: same volume, p. 346).

Rosenfeld, H.D. and Holstein, W.L. (1999) Correlation of predicted and measured iron oxidation states in mixed iron oxides. DND-CAT 1999 activity report, Agornne National Laboratory, Argonne (Il), U.S.A.

Rossano, S., Balan, E., and Brouder, C. (1999) ⁵⁷Fe Mössbauer spectroscopy of tektites. Physics and Chemistry of Minerals, 26, 530–538

Rossano, S., Ramos, A.Y., and Delaye, J.-M (2000) Environment of Fe²⁺ iron in CaFeSi₂O₆ glass; contributions of EXAFS and molecular dynamics. Journal of Non-Crystalline Solids, 273, 48–52.

Seifert, F. and Olesch, M. (1977) Mössbauer spectroscopy of grandidierite, (Mg,Fe)Al₃SiO₉. American Mineralogist, 62, 547–553.

Sobolev, V.N., McCammon, C.A., Taylor, L.A., Snyder, G.A., and Sobolev, N.V. (1999) Precise Mössbauer milliprobe determination of Fe³⁺ iron in rock-forming minerals and limitations of electron microprobe analysis. American Mineralogist, 84, 78–85.

Solé, A.V., Gauthier, C., Goulon, J., and Natali, F. (1999) Undulator QEXAFS at the ESRF beamline ID26. Journal of Synchrotron Radiation, 6, 174–175.

Stephenson, D.A. and Moore, P.B. (1968) The crystal structure of grandidierite, (Mg,Fe)Al₃SiBO₉. Acta Crystallographica B, 24, 1518–1522.

Srivastava, U.C. and Nigam, H.L. (1973) X-ray absorption edge spectrometry (XAES) as applied to coordination chemistry. Coordination Chemistry Reviews, 9, 275–310.

Tröger, L., Arvanitis, D., Baberschke, K., Michaelis, H., Grimm, U., and Zschech, E. (1992) Full correction of the self-absorption in soft-fluorescence extended

X-ray-absorption fine structure. Physical Review B, 46, 3283–3289.

Valley, J.W., Peacor, D.R., Bowman, J.R., Essene, E.J., and Allard, M.J. (1985) Crystal chemistry of a Mg-vesuvianite and implications of phase equilibria in the system CaO-MgO-Al$_2$O$_3$-SiO$_2$-H$_2$O-CO$_2$. Journal of Metamorphic Geology, 3, 137–153.

Van Aken, P.A., Liebscher, B., and Styrsa, V.J. (1998) Quantitative determination of iron oxidation states in minerals using Fe L$_{2,3}$-edge electron energy-loss near-edge structure spectroscopy. Physics and Chemistry of Minerals, 25, 323–327.

Van Aken, P.A., Styrsa, V.J., Liebscher, B., Woodland, A.B., and Redhammer, G.J. (1999) Microanalysis of Fe^{3+}/?Fe in oxide and silicate minerals by investigation of electron energy-loss near-edge structures (ELNES) at the Fe M$_{2,3}$ edge. Physics and Chemistry of Minerals, 26, 584–590.

Waychunas, G.A. (1983) Mössbauer, EXFAS and X-ray diffraction study of Fe^{3+} clusters in MgO:Fe and magnesiowüstite (Mg,Fe)$_{1-x}$O: evidence for specific cluster geometries. Journal of Materials Science, 18, 195–207.

Waychunas, G.A. and Rossman, G.R. (1983) Spectroscopic standard for tetrahedrally coordinated Fe^{3+} iron: γ-LiAlO$_2$: Fe^{3+}. Physics and Chemistry of Minerals, 9, 212–215.

Waychunas, G.A., Apted, M.J., and Brown, G.E. Jr. (1983) X-ray K-edge absorption spectra of Fe minerals and model compounds: near edge structure. Physics and Chemistry of Minerals, 10, 1–9.

Waychunas, G.A., Dollase, W.A., and Ross, C.R. (1994) Short-range order measurements in MgO-FeO and MgO-LiFeO$_2$ solid solutions by DLS simulation-assisted EXAFS analysis. American Mineralogist, 79, 274–288.

Weber, H.P. and Hafner, S.S. (1971) Vacancy distribution in nonstoichiometric magnetites. Zeitschrift für Kristallographie, 133, 327–340.

Westre, T.E., Kennepohl, P., de Witt, J., Hedman, B., Hodgson, K.O., and Solomon, E.I. (1997) A multiplet analysis of Fe K-edge 1s → 3d pre-edge features of iron complexes. Journal of the American Chemical Society, 119, 6297–6314.

White, W.B. (1966) Optical absorption spectra of iron in the rock-forming silicates. American Mineralogist, 51, 774–791.

White, E.H. and McKinstry, H.A. (1966) Chemical effect on X-ray absorption-edge fine structure. Advances in X-ray Analysis, 9, 376–392

White, W.B, Matsumura, M., Linnehan, D.G., Furukawa, T., and Chandrasekhar, B.K. (1986) Absorption and luminescence of Fe^{3+} in single-crystal orthoclas. American Mineralogist, 1986, 71, 1415–1419.

Wilke, M., Farges, F., Behrens, H., and Burkhard, D. (1999) The effect of water on the local environment of Fe in silicate glasses. European Journal of Mineralogy, 11, suppl. 1, 244.

Wood, B.J. and Virgo, D. (1989) Upper mantle oxidation state: Fe^{3+} iron contents of lherzolite spinels by ^{57}Fe Mössbauer spectroscopy and resultant oxygen fugacities. Geochimica et Cosmochimica Acta, 53, 1277–1291.

Wu, C.C. and Mason, T.O. (1981) Thermopower measurement of cation distribution in magnetite. Journal of the American Ceramic Society, 64, 520–522.

Wu, Z.Y., Ouvrard, G., and Natoli, C.R. (1996) Study of pre-edge structures in the K-edge XANES/ELNES spectra of some transition-metal oxides and sulfides. Journal de Physique IV, 7, 199–201.

Yamamoto, A. (1982) Modulated structure of wustite (Fe$_{1-x}$O) (three-dimensional modulation). Acta Crystallographica B, 38, 1451–1456.

Yang, H. and Smyth, J.R. (1996) Crystal structure of a P2$_1$/m ferromagnesian cummingtonite at 140 K. American Mineralogist, 81, 363–368.

Zhang, L., Ahsbahs, H., Hafner, S.S., and Kutoglu, A. (1997) Single-crystal compression and crystal structure of clinopyroxene up to 10 GPa. American Mineralogist, 82, 245–258.